Development of Pulse Shape Discrimination Techniques for Tritium Production Rate and Fast Neutron Flux Measurement Using a Single Crystal Diamond Based Radiation Detector for the Application of Breeding Blanket Performance Experiments

Makoto I. KOBAYASHI[1,2)]*, Sachiko YOSHIHASHI[3)], Kunihiro OGAWA[1,2)], Mitsutaka ISOBE[1,2,4)], Masaki OSAKABE[1,2)]

[1)] *National Institute for Fusion Science, National Institutes of Natural Sciences, Toki 509-5292, Japan*
[2)] *The Graduate University for Advanced Studies, SOKENDAI, Toki 509-5292, Japan*
[3)] *Graduate School of Engineering, Nagoya University, Furo-cho, Nagoya 464-8603, Japan*
[4)] *Department of Physics, Mahasarakham University, Maha Sarakham 44150, Thailand*

(Received 31 March 2025 / Accepted 11 January 2026)

In this study, we present a comprehensive description of a single crystal diamond-based detector (SCDD) system equipped with a ^{6}Li thermal neutron converter and its radiation detection processes. Based on these processes, several pulse shape discrimination (PSD) methods applicable to the performance evaluation of breeding blankets are proposed. A basic PSD method, using either pulse width or charge integral alone, enables discrimination between gamma-rays and energetic ions produced by the ^{6}Li(n,α)^{3}H reaction. This method is therefore suitable for measuring the tritium production rate in a thermal neutron irradiation field. An advanced PSD method, utilizing both pulse width and a specific pulse shape index, effectively rejects gamma-ray signals and extracts pulses originating from fast neutrons and energetic ions produced by the ^{6}Li(n,α)^{3}H reaction. Post-analysis of the extracted signals demonstrates that both the tritium production rate and the fast neutron flux can be evaluated simultaneously in a mixed radiation field using a single SCDD. In addition to the intrinsic advantages of SCDD, such as compact size, excellent radiation hardness, and high temperature operability, the PSD methods developed in this study enable broader applications not only in breeding blanket performance evaluation but also across a wide range of scientific research fields.

Keywords: tritium, neutron, breeding blanket, diamond detector

DOI: 10.1585/pfr.21.1505020

1. Introduction

Deuterium (D)-Tritium (T) is one of the most promising fuel combinations for fusion reactors due to its high reaction cross-section at relatively lower temperatures [1–3]. However, tritium rarely exists in the environment. Therefore, it must be generated within the fusion reactor itself. The breeding blanket (BB) is designed to generate fuel tritium and is positioned to surround the burning plasma, receiving fast neutrons [4–8]. Fast neutrons are scattered by collisions with the structural and loaded compounds of the BB, causing them to decelerate. Lithium-based compounds are loaded into the BB to produce tritium through the ^{6}Li(n,α)^{3}H reaction [9–12]. These processes convert the kinetic energy of fast neutrons into heat, which is then utilized for power generation. Additionally, the blanket functions as a neutron shield for the superconducting coils located outside the blanket.

A variety of blanket concepts have been proposed, utilizing different tritium breeding materials and coolant combinations, such as water-cooled ceramic breeders, helium-cooled ceramic breeders, self-cooled liquid breeders, and so on [13–20]. The structural designs of BBs have been developed to ensure tritium self-sufficiency, first wall cooling, and efficient heat transfer. All these designs rely on advanced neutron transport calculation software and nuclear data libraries [21–25]. However, it is well known that nuclear data libraries contain uncertainties, and neutron transport models are not entirely rigorous. Additionally, impurities within BB components can affect neutron transport properties. These unavoidable factors can influence BB performance, particularly the tritium breeding rate, reactor operational scenarios, plant costs, and nuclear waste production. Therefore, it is essential to compare computational predictions with experimental measurements, such as fast neutron flux and tritium production rate,

**Corresponding author's e-mail: kobayashi.makoto@nifs.ac.jp*
This article is based on the invited talk at the 41st JSPF Annual Meeting (2024, Tokyo).

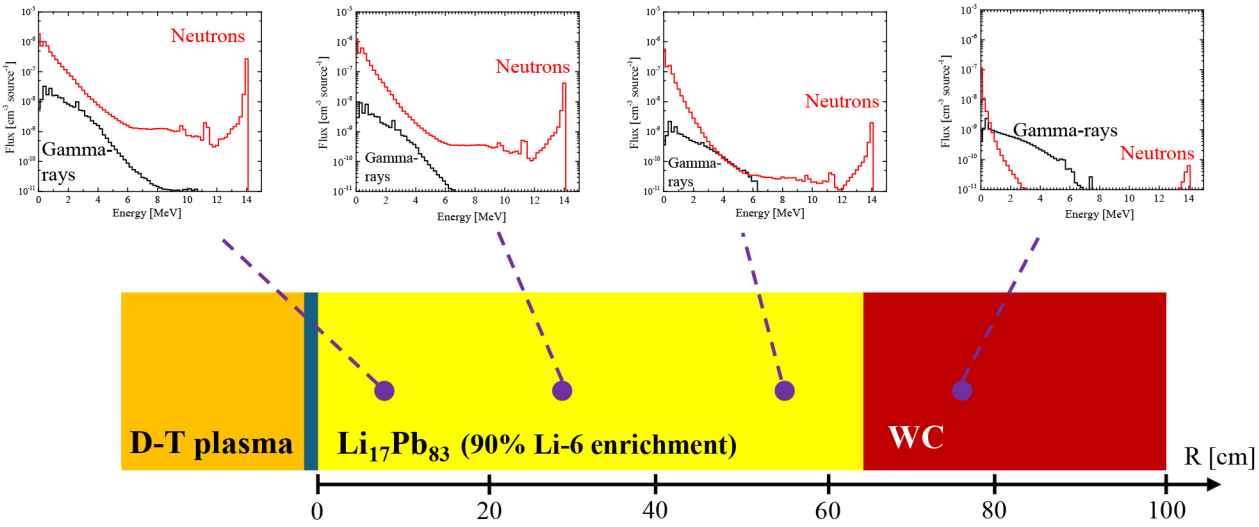

Fig. 1. Radiation spectrum in the radial-build model blanket composed of low activation ferritic steel, lead-lithium (90% Li-6 enrichment) and tungsten carbide, estimated by the Particle and Heavy Ion Transport code System (PHITS) code. The ENDF/B-VII.1 Evaluated Nuclear Data Library is used. The radiation spectrum was estimated by T-track tally. Note that the configuration shown here is a generic modeling example for demonstration purposes and is not based on any particular engineering design or project.

using a blanket mock-up.

For these performance test experiments, a sensor capable of detecting both tritium generation and fast neutrons is necessary. Figure 1 displays a typical radiation flux distribution in the blanket. In this figure, the blanket is modeled as a radial-build system using a lead-lithium eutectic alloy as the tritium breeder, while tungsten carbide serves as the shielding blanket (SB). The structural material is reduced activation ferritic steel [26, 27]. About 14 MeV neutrons are generated in the plasma region and transported to the blanket region. It is well known that neutrons can be captured by specific elements, emitting prompt gamma-rays. Thus, gamma-rays are always associated with neutron interactions. A significant fast neutron flux is expected near the plasma region. The fast neutron component decreases in deeper regions, whereas lower energy neutron components increase due to neutron scattering. Gamma-rays below 8 MeV are always observed, and their relative flux increases compared to neutrons in deeper blanket regions. These estimations clearly indicate a wide flux distribution of neutrons, ranging from thermal neutrons to 14 MeV neutrons. Additionally, gamma-ray flux cannot be ignored. This suggests that a detector for BB performance tests must quantitatively measure the tritium production rate and fast neutron flux under gamma-ray irradiation conditions.

To meet these requirements, we have evaluated the capabilities of single crystal diamond based radiation detectors (SCDD) [28, 29]. Single-crystal diamond (SCD) is a semiconductor. The SCDD is developed by equipping an SCD with electronic circuits, allowing it to function as a radiation detector capable of detecting fast neutrons. Additionally, the SCDD can detect bred tritium by placing a thin lithium compound foil in front of the SCD. The details of these radiation detection processes will be explained later. Despite these attractive radiation detection capabilities, the SCDD can also detect gamma-rays. Hence, a discrimination method to differentiate fast neutrons, bred tritium, and gamma-rays is necessary. To address this, we have developed the pulse shape discrimination (PSD) method to separately measure each type of radiation using the SCDD.

This paper reviews our development of PSD methods. We began with a primitive PSD method to separate energetic ions and gamma-rays, and concluded with the eventually achieved successful PSD method of quantitative and simultaneous PSD method for measurements of the tritium production rate and fast neutron flux. In this paper, we describe the principle of the PSD method and summarize benchmark experimental results. This paper covers not only recent advancements in the PSD method but also earlier, more primitive PSD methods, as these approaches remain useful for various applications. Finally, we discuss remaining challenges in these developments.

2. Single-Crystal Diamond-Based Radiation Detector

2.1 Characteristics of single-crystal diamond

The SCD is a semiconductor material that has gained attention not only for radiation detection but also for applications in material processing, power electronics, and optics [30]. Recent advancements in chemical vapor deposition (CVD) techniques have enabled the production of detector-grade SCD [31]. Nowadays, SCDD is commercially available at a reasonable price [32, 33].

The SCDD is a type of semiconductor radiation detector. The size of an SCDD assembled with detector-grade SCD is usually less than 10 cm^3. SCDD has been proposed for various applications due to its compact size and excellent properties, such as high radiation tolerance, high temperature operation capability, high energy resolution, and so on. Table 1 compares some fundamental and electronic properties of SCD with

Table 1. Electronic properties of diamond compared to silicon.

Property	Diamond	Silicon
Band gap energy [eV]	5.5	1.12
Electron mobility [$cm^2\ V^{-1}\ s^{-1}$]	1,800	1,500
Hole mobility [$cm^2\ V^{-1}\ s^{-1}$]	2,500	450
Intrinsic carrier density [cm^{-3}]	$< 10^3$	$\sim 10^{10}$
Atomic number	6	14
Mass density [$g\ cm^{-3}$]	3.52	2.33
Displacement energy [eV]	37.5–47.6	13–20
Energy to create one e-h pair [eV]	13	3.6

those of silicon, which is a typical semiconductor material [34–38]. For example, SCD has been considered for tissue-equivalent X-ray dose monitoring in radiation therapy, as its effective atomic number (Z) is close to that of the human body's constituent atoms [39]. Another advantage of SCDD is its radiation hardness. For instance, SCDD has been used as a beam-loss monitor in high-energy physics experiments, where high radiation tolerance and excellent time resolution are required [40–42]. The wide bandgap of SCD allows SCDD to operate without cooling, making it compact and easy to install in confined spaces or transport through narrow ports into intense radiation fields, minimizing occupational exposure.

The application of SCDD for fusion reactor development has also been explored [43]. Its potential uses include fusion plasma diagnostics, such as a neutral particle analyzer [44–46] and a recoiled proton detector [47, 48]. Additionally, SCDD has been employed to measure the ion temperature of D-T burning plasma through neutron energy spectrum broadening, taking advantage of its excellent energy resolution [49–55]. Recently, SCDD has been investigated for reaction product measurements in the p-^{11}B fusion system [56].

SCDD is also proposed for blanket performance diagnostics due to its radiation hardness and high-temperature operation capabilities. To assess these properties, high-dose 14 MeV neutron irradiation and high-temperature tolerance experiments have been conducted. Moreover, an SCDD equipped with a lithium fluoride (^{6}LiF) thin foil, with ~ 95% ^{6}Li enrichment, has been developed for bred tritium measurement. In this setup, the ^{6}Li in the foil primarily reacts with thermal neutrons through the ^{6}Li(n,α)^{3}H reaction, producing energetic tritons and alpha particles that deposit kinetic energy into the SCD for detection [57–62]. This method is also utilized in the present study and will be introduced later.

2.2 The single crystal diamond detector and data acquisition systems

The SCDD used in this study includes a B-12 Knof diamond detector [63] and a B-6 high-temperature thermal neutron detector [64], both manufactured by Cividec Instrumentation GmbH [32]. The SCD in the SCDD has dimensions of 4.5 × 4.5 mm^2 and a thickness of 0.5 mm, resulting in an active volume of 4.0 × 4.0 × 0.5 mm^3. A thin metal titanium layer with the thickness of 100 nm is deposited on both surfaces of the SCD to serve as electrodes. Due to its extremely low impurity concentration, the SCD is fully depleted under the applied bias voltage, and the entire crystal acts as an active charge collection region. The SCD is housed within a casing to form an electrical circuit for detection.

The ^{6}LiF foil is used for the tritium production rate measurement. The thickness of the foil is typically 1.9 μm. The foil is fixed on the substrate and faced to the SCD so that

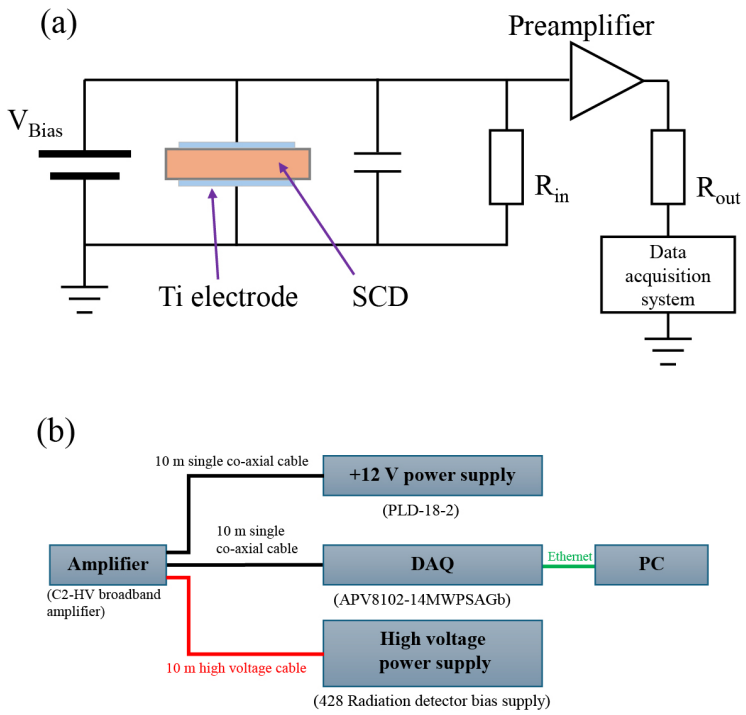

Fig. 2. The schematic image of (a) the equivalent circuit diagram of the SCDD system with a current amplifier, and (b) the layout of electronic components.

energetic tritons generated in the foil can transport into the SCD to deposit energy.

Figure 2(a) displays an equivalent circuit diagram of the SCDD system. The SCDD operates in current amplifier mode using a CIVIDEC C2-HV broadband amplifier. Figure 2(b) shows the layout of the electronic components [35, 36, 65]. The amplified signal is transmitted to a data acquisition system (Techno AP APV8102-14MWPSAGb), which consists of a fast-processing analog-to-digital converter (ADC) and a field-programmable gate array (FPGA) [66]. The system has a sampling rate of 1 GHz and a resolution of 14 bits. The current amplifier is powered by a +12 V DC power supply (Matsusada Precision PLD-18-2). The bias voltage is applied to the SCDD electrode from a high-voltage power supply (ORTEC 428) through the amplifier. These instruments are connected using coaxial cables, each measuring 20 meters or less in length.

2.3 The radiation detection mechanism of the SCDD

Electrons in the SCD crystal structure typically occupy the valence band, making SCD an insulator in its default state. When radiation interacts with the SCD, it deposits energy, exciting electrons from the valence band to the conduction band. These excited electrons, now free to move within the crystal, leave behind positively charged holes. This process is known as electron-hole pair creation. Free electrons move toward the positively charged electrode, while holes migrate toward the negatively charged electrode when an external electric field is applied. This motion induces a current in the circuit [67].

The phenomenon in which current is induced by the movement of electron-hole pairs under an applied electric field is well explained by the Shockley-Ramo theorem [68, 69]. When an electric field is applied to one electrode of the SCD while the other is grounded, electrons and holes drift towards opposite electrodes due to the Lorentz force. Assuming a point-like charge distribution in the SCD, parallel planar electrodes, and the absence of a magnetic field, the following equation describes the Lorentz force:

$$F = q_0 E, \tag{1}$$

where F is the Lorentz force, q_0 is the point-charge, and E is the electric field. Given the applied voltage V_0 and the distance between parallel planar electrodes, d, the electric field can be expressed as:

$$E = \frac{V_0}{d}. \tag{2}$$

According to the Schockley-Ramo theorem, the instantaneous current $I(t)$ induced on the electrodes can be expressed using the drift velocity of the charge υ_{drift} as follows,

$$I(t) = \frac{q_0 N}{d}\upsilon_{drift}. \tag{3}$$

Here, N is the number of charge carriers in this point, and $\upsilon_{drift} = \mu E$, where μ is a mobility of the charge in the SCD.

The total number of drifting charges can be determined by integrating the current.

$$Q = \int I(t)\,dt. \tag{4}$$

In the actual event, the current is the sum of contributions from both electron and hole drift. If ionization events occurred as point-like at the depth x of the SCD, and the negative voltage is applied on the electrode ($x = 0$), the electron collection time (τ_e) and the hole collection time (τ_h) can be defined as,

$$\tau_e = \frac{d-x}{\upsilon_e},\ \tau_h = \frac{x}{\upsilon_h}. \tag{5}$$

Initially, when ionizing radiation generates electron-hole pairs, the induced current is zero. Then, the drifts of electrons and holes produce the induced current, which eventually reaches $q_0 N$ when all electrons and holes are totally collected. In summary, time-dependent induced charge $Q(t)$ can be decomposed to following forms according to the drift time of electrons and holes [67],

$$Q(t) = q_0 N\left(\frac{\upsilon_e}{d}t + \frac{\upsilon_h}{d}t\right),\ (t < \tau_e, t < \tau_h), \tag{6}$$

$$Q(t) = q_0 N\left(\frac{\upsilon_e}{d}t + \frac{x}{d}\right),\ (\tau_h < t < \tau_e), \tag{7}$$

$$Q(t) = q_0 N\left(\frac{d-x}{d} + \frac{\upsilon_h}{d}t\right),\ (\tau_e < t < \tau_h), \tag{8}$$

$$Q(t) = q_0 N,\ (t > \tau_e, t > \tau_h). \tag{9}$$

The last equation indicates that the overall time-integrated induced current is proportional to the total charge in the SCD, meaning the energy transferred by ionizing particles to the SCD can be determined, provided charge losses during drift are negligible. Since detector-grade SCDs have minimal impurities and structural defects, the induced charge can be used to estimate ionizing particle energy.

The above analyses assumed with the point-like electron-hole pair distribution in the SCD, which can be applicable for bred tritium and fast neutron irradiation. On the other hand, gamma-ray irradiation tends to produce a more scattered electron-hole pair distribution in the SCD. To cover these cases, the induced current is given by the following generalized form,

$$I(t) = \int q_0 N_h(x,t)\frac{\upsilon_h}{d}\,dx + \int q_0 N_e(x,t)\frac{\upsilon_e}{d}\,dx. \tag{10}$$

This equation takes the initial distribution of electron-hole pairs in the SCD into account. Note that the point charge of electrons is equivalent to holes, and the initial distribution of electron is the same as holes ($N_h(x, 0) = N_e(x, 0)$). Despite its complexity, this equation still implies that the total induced charge remains proportional to the deposited energy.

2.4 Interactions of the SCD with radiation

The generalized form of induced current equation

indicates that the waveform of the induced current depends on the initial distribution of electron-hole pairs in the SCD. In this section, the distribution of electron-hole pairs induced by various types of radiation is evaluated. For this evaluation, the radiation transport code PHITS is used. Three types of radiation are examined: a 2.7 MeV triton, a 7.6 MeV gamma-ray, and a 14 MeV neutron. The energy of the energetic triton originates from the Q-value of ^{6}Li(n,α)^{3}H reaction. The 7.6 MeV gamma-rays corresponds to the prompt gamma-ray energy in ^{56}Fe(n,γ)^{57}Fe reaction [70]. This gamma-ray should be prominent because iron is the major element of the structural material of the BB, the reaction has one of the highest emission probabilities of ^{56}Fe which is the most abundant natural isotope of iron. The 14 MeV neutrons are the product of D-T fusion reaction. In the PHITS code, a pencil-shaped beam of each-type of radiation is injected perpendicularly into the major surface of SCD, with the same dimension in Sec. 2.1.

The transport behavior of each type of radiation is illustrated in Fig. 3. The trajectories from 10^4 individual runs are superimposed in this figure. The region from −0.05 to 0 cm along the z-axis consists of the SCD, while the region where $z > 0$ cm is vacuum. In the case of 2.7 MeV triton irradiation, the penetration range is limited to the shallow region of the SCD. Traveling energetic ions interact with electrons in the material via Coulomb forces, significantly hindering their transport and resulting in a short range within the material. Unlike triton irradiation, gamma-rays and neutrons are electrically neutral, leading to distinct transport behaviors. In both cases, most radiation passes through the SCD without interacting. However, radiation scattering occasionally occurs at random depths within the SCD, indicating energy deposition events that may be detectable in the SCDD.

Energetic triton irradiation deposits energy directly into the SCD through energy transfer from the triton to the SCD. In contrast, energy deposition mechanisms for gamma-rays and neutrons differ. Gamma-ray irradiation induces several processes within the SCD, including the photoelectric effect, pair production, and Compton scattering [67]. In each process, gamma-ray energy is transferred to electrons, which subsequently deposit energy into the SCD. Fast neutron irradiation induces nuclear reactions in the SCD such as ^{12}C(n,α)^{9}Be, ^{12}C(n,n'2α)α and ^{12}C(n,n')^{12}C reactions, [24, 25], generating energetic ions which in turn deposit energy into the material.

To visualize energy deposition behaviors for each type of radiation, the ranges of electrons and energetic ions in the SCD are investigated and summarized in Fig. 4. This figure evaluates the ranges of four charged particles in the SCD as a function of their initial energy. The results for tritons indicate that the range of a 2.7 MeV triton is less than 20 μm, consistent with Fig. 3(a). The energy range of alpha particles in this figure corresponds to the reaction products of two nuclear reactions: the ^{6}Li(n,α)^{3}H reaction with thermal neutrons (minimum energy) and the ^{12}C(n,α)^{9}Be reaction with 14 MeV neutrons (maximum energy), as evaluated by PHITS. Even for an 8 MeV alpha particle, the range is less than 20 μm. The range of ^{12}C ions is also evaluated, as these energetic ions are likely produced via the elastic collisions of fast neutrons with carbon atoms in the SCD. The maximum ^{12}C energy of ~ 4 MeV shown in Fig. 4 is derived from neutron slowing-down theory [71, 72]. The results indicate that ^{12}C ions have

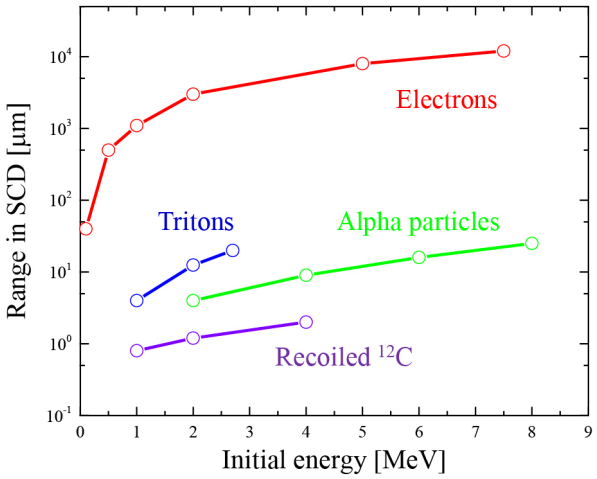

Fig. 4. The transport ranges of energetic particles in the SCD as a function of initial energy.

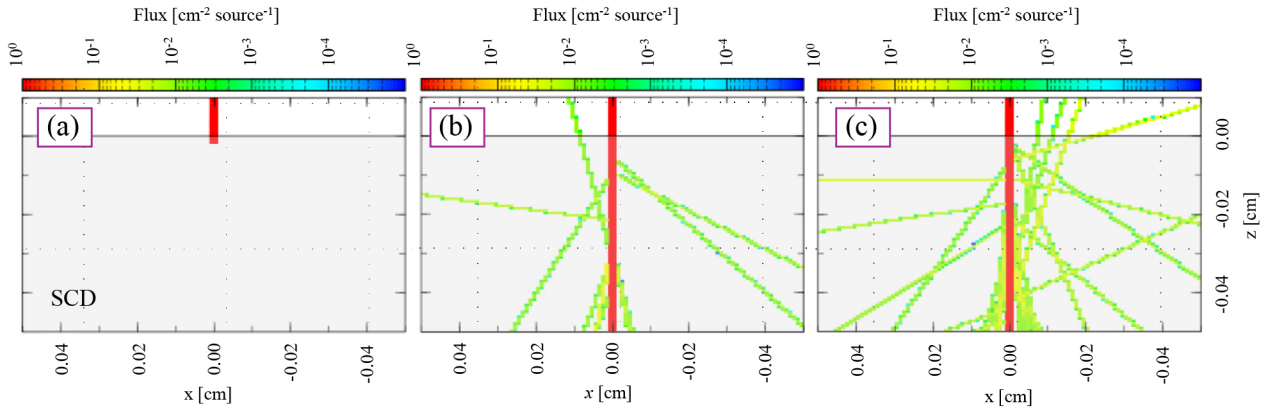

Fig. 3. Radiation tracks in (a) 2.7 MeV triton, (b) 7.6 MeV gamma-ray, and (c) 14.1 MeV neutron irradiation into the SCD estimated by T-track tally of PHITS code. The gray area and the white area represent the SCD and the vacuum region, respectively. The results of 10^4 single runs of each radiation transport simulation are superposed. The color map represents each radiation flux in these figures.

a much shorter range due to their higher charge density compared to tritons and alpha particles.

The results for electrons exhibit a markedly different trend. The maximum electron energy of ~ 7.3 MeV shown in Fig. 4 corresponds to the maximum energy transfer in the Compton scattering process by 7.6 MeV gamma-ray irradiation. Even for a 1 MeV electron, the range exceeds 1,000 μm. Because the thickness of the SCD used in this work is 500 μm (see Sec. 2.1), scattered electrons can penetrate through a broad region of the SCD. A single scattered electron can induce additional electron scattering events. The long trajectory of scattered electrons suggests widespread energy deposition throughout the SCD thickness.

Based on the evaluation of radiation transport and the subsequent transport of induced charged particles within the SCD, the differences in energy deposition distributions for each type of radiation can be summarized as follows:

1. Energetic triton irradiation (for tritium production rate measurement): Energy deposition occurs only in the shallow region of the incident surface of SCD. Consequently, the distribution of electron-hole pairs in each energetic triton irradiation event is localized near the incident surface of the SCD.
2. Gamma-ray irradiation: Energy transfer from gamma-rays to electrons occurs at random depths within the SCD. Scattered electrons travel over a wide region, generating secondary scattering. Ultimately, electron-hole pairs are distributed throughout the entire thickness of the SCD in each gamma-ray irradiation event.
3. Fast neutron irradiation (for fast neutron flux measurement): Nuclear reactions occur randomly at various depths within the SCD, producing energetic ions that can travel with very short ranges in the SCD. As a result, electron-hole pair distributions appear as point-like clusters at different depths within the SCD for each fast neutron irradiation event.

These differences in the initial electron-hole pair distribution induced by each type of radiation should be reflected in the waveform of the induced current in the SCDD, suggesting that events caused by different types of radiation can be distinguished based on the waveform of the induced current.

3. Demonstration of Discriminative Radiation Measurements

3.1 Energetic triton and gamma-ray discrimination [61, 62, 73, 74]

3.1.1 Estimation of pulse shapes

In the deeper region of the BB, most fast neutrons have been moderated, making thermal neutrons the dominant neutron energy level. In this region, the tritium production rate can be measured by discriminating induced pulses in the SCDD between those caused by energetic tritons and gamma-rays. Energetic triton production primarily occurs through the ^{6}Li(n,α)^{3}H reaction, whose cross-section increases inversely with neutron energy [24, 25]. Therefore, detecting energetic tritons can be utilized for thermal neutron flux measurements. This application can be used, for example, in radiation safety and control at nuclear facilities.

According to the discussion in Sec. 2.4, the electron-hole pair distribution in the SCD induced by energetic triton irradiation should be localized near the incident surface, whereas electron-hole pairs induced by gamma-ray irradiation should be widely distributed throughout the entire thickness of the SCD. Here, the waveforms (pulse shapes) of the induced current in each event are estimated based on the equations derived in Sec. 2.3.

Given that a negative voltage is applied to the incident surface of the SCD, induced electrons drift toward the rear-side electrode, while induced holes drift toward the incident surface electrode. In the case of energetic triton irradiation, the hole collection time is significantly shorter than the electron collection time ($\tau_h \ll \tau_e$) due to the much shorter drift distance. When a positive voltage is applied to the incident surface, this relationship reverses ($\tau_e \ll \tau_h$). The estimated waveform of the induced current in this case is shown in Fig. 5(a). In this estimation, the alpha particle is injected into the positively charged incident surface of the SCD at 10 ns, and both the rise time and fall time of the detector response are ignored. In this case, the electron collection time is shorter than the sampling rate of the data acquisition system. Therefore, the current induced by the electron drift cannot be detected. Consequently, the pulse shape is primarily determined by the drift of a single charge carrier type (holes in this case), it exhibits a rectangular shape with a wide pulse width.

For the estimation of the pulse shape in gamma-ray irradiation, a uniform distribution of electron-hole pairs throughout the entire depth of the SCD is assumed as a simplified model. The estimated pulse shape is shown in Fig. 5(b). The same assumptions as in Fig. 5(a) are applied in this calculation. The resulting pulse shape is triangular, formed by the superposition of induced currents due to the drift of both electrons and holes.

3.1.2 Pulse shape discrimination method based on the pulse width

The estimation of pulse shapes in energetic triton and gamma-ray irradiation showed that the pulse shapes differ at certain points, making pulse shape discrimination possible.

The first attempt at PSD is based on the pulse width. As shown in Fig. 5, the difference in pulse shapes (rectangular or triangular) reflects in the pulse width. The pulse width, such as the Full-Width at the Half-Maximum (FWHM), for each pulse event can be evaluated as follows. Given that the single pulse data, after background current subtraction, forms a vector $\boldsymbol{\zeta}$:

$$\boldsymbol{\zeta_j} = \{a_{0,j}, a_{1,j}, \cdots, a_{i,j}, \cdots, a_{k,j}, \cdots, a_{T-2,j}, a_{T-1,j}\}. \quad (11)$$

Here, i and j represent the time index and the event number, respectively. T is the number of elements in this vector. First, the time index at the highest current is determined. Here we assume that $a_{k,j}$ = arg.max($\boldsymbol{\zeta_j}$). Then, the time indices at half-

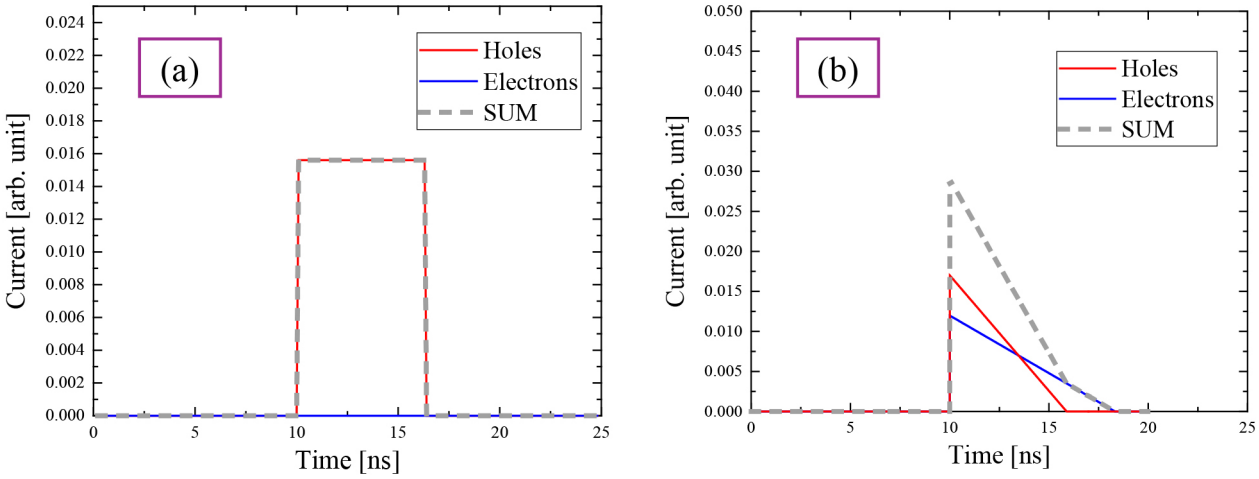

Fig. 5. The predicted waveform of induced current in the SCDD by the irradiation of (a) an alpha particle and (b) a gamma-ray. The applied voltage of −400 V on the rear surface electrode is assumed. Each radiation injected at the time of 10 ns. The rise-time and the fall-time of the SCDD were ignored in these predictions.

height, both before and after the highest current, are evaluated to determine the FWHM.

$$\boldsymbol{\eta_{L,j}} = \{(a_{0,j}-\delta_j)(a_{1,j}-\delta_j),(a_{1,j}-\delta_j)(a_{2,j}-\delta_j), \cdots,(a_{k-1,j}-\delta_j)(a_{k,j}-\delta_j)\}, \quad (12)$$

$$\boldsymbol{\eta_{R,j}} = \{(a_{k,j}-\delta_j)(a_{k+1,j}-\delta_j), \cdots,(a_{T-2,j}-\delta_j)(a_{T-1,j}-\delta_j)\}' \quad (13)$$

$$(\mathrm{FWHM})_j = arg.min(\boldsymbol{\eta_{R,j}}) - arg.min(\boldsymbol{\eta_{L,j}}). \quad (14)$$

Here, δ_j is equivalent to $a_{k,j}/2$. Other pulse width value can be evaluated in the same manner. For example, when evaluating the FW1/4PH (Full-Width of one-fourth of the Peak Height), δ_j should be $a_{k,j}/4$.

After evaluating the FWHM for pulse dataset consisting of events induced by energetic triton and gamma-ray irradiation, the histogram of FWHM will show a bimodal distribution. Events with shorter FWHM correspond to gamma-rays, while events with wider FWHM originate from energetic tritons. This enables the discrimination of each type of radiation.

3.1.3 Pulse shape discrimination method based on charge-integral

The PSD method using pulse width was introduced in Sec. 3.1.2. This method works for separating energetic tritons and gamma-rays. However, the evaluation process of pulse width in this method may be relatively influenced by the signal fluctuation. The charge-integral method is an alternative that offers advantages, such as fast processing and stability against signal fluctuations. As in Sec. 3.1.2, we assume the single pulse data forms a vector $\boldsymbol{\zeta}$. The time index where the pulse begins is usually different in each pulse. Therefore, the time index at which the current begins to rise (t_j^{start}) is determined. A similar method to the one in Sec. 3.1.2 can be applied.

$$\boldsymbol{\eta_{L,j}} = \{(a_{0,j}-\delta_{th})(a_{1,j}-\delta_{th}),(a_{1,j}-\delta_{th})(a_{2,j}-\delta_{th}), \cdots,(a_{k-1,j}-\delta_{th})(a_{k,j}-\delta_{th})\}, \quad (15)$$

$$t_j^{start} = arg.min(\boldsymbol{\eta_{L,j}}). \quad (16)$$

Here, $a_{k,j}$ = arg.max($\boldsymbol{\zeta_j}$) is assumed. The factor δ_{th} is the threshold current, which is a constant value slightly higher than the background current. Next, the following two parameters are calculated.

$$Q_j^{fast} = \int_{t_j^{start}-w}^{t_j^{start}+w} a_{i,j}\,dt, \quad (17)$$

$$Q_j^{total} = \int_{t_j^{start}-w}^{T-1} a_{i,j}\,dt. \quad (18)$$

Q^{total} corresponds to the total charge in the event, and w is a constant with the range of $0 < w < k$. As mentioned in Sec. 3.1.1, the pulse shape induced by the energetic triton irradiation should have a wide plateau region, while the pulse shape induced by gamma-ray irradiation decreases quickly after the peak. This suggests that the value of Q_{fast}/Q_{total} in the former case should be smaller, whereas Q_{fast}/Q_{total} should be larger in the latter case. Similar to the PSD method using pulse width, the histogram of Q_{fast}/Q_{total} for the pulse dataset consisting of events induced by energetic triton irradiation and gamma-ray irradiation will show a bimodal distribution. Hence, events with larger Q_{fast}/Q_{total} are caused by gamma-rays, and events with smaller Q_{fast}/Q_{total} are from energetic tritons, enabling the discrimination of each type of radiation.

3.1.4 Demonstration of energetic triton measurement under gamma-ray irradiation environment

In this section, PSD methods to evaluate energetic triton measurements under gamma-ray irradiation environment are demonstrated. Before this demonstration, fundamental experiments using radiation sources were conducted to assess the performance of PSD methods. The radiation sources of ^{241}Am and ^{60}Co were used, which emit alpha particles (~ 5.5 MeV) and gamma-rays (1.17 and 1.33 MeV), respectively. As shown in Fig. 4, the range of ~ 5.5 MeV alpha particles in the SCD is similar to that of 2.7 MeV energetic tritons. These

radiation sources were placed in front of the surface of the SCD in the SCDD, simultaneously irradiating both alpha particles and gamma-rays into the SCDD. The details of experiments can be found elsewhere [73].

The histogram of FWHM distribution of pulses in this measurement is displayed in Fig. 6. As discussed above, the FWHM distribution was bimodal characteristic, indicating the region with shorter FWHM is caused by gamma-rays, while the region with wider FWHM originates from alpha particles. Figure 7 presents the results of PSD method using charge-integral from the same experiment. This figure summarizes the Q_{total} as a function of Q_{fast}/Q_{total}, making the discrimination between pulses induced by alpha particles and gamma-rays more apparent. Figure 8 shows a typical pulse induced by an alpha particle and a gamma-ray, discriminated by PSD methods described above. The pulse shape was consistent with the prediction shown in Fig. 5. It can be concluded that both PSD methods are effective for discriminating pulses induced by alpha particles from those by gamma-rays. Accordingly, the discrimination of pulses induced by energetic tritons from those by gamma-rays should also be feasible.

The demonstration of the PSD method to separately measure pulse events by energetic tritons under gamma-ray irradiation environments was carried out using a ^{252}Cf spontaneous neutron source. A storage box made of lead, polyethylene and concrete, containing a 260 MBq ^{252}Cf, released slowing-down neutrons associated with gamma-rays. The SCDD equipped with ^{6}LiF foil was placed next to the storage box to be irradiated with neutrons and gamma-rays. The details of the experiment can be found elsewhere [73].

Pulses obtained in this experiment were analyzed using the PSD method based on the pulse width. Then, Q_{total} of pulses with shorter FWHM and Q_{total} of pulses with wider FWHM were evaluated. The histogram of Q_{total}, known as the total charge spectrum as in Eq. (9), is displayed in Fig. 9. The total charge spectrum of all pulses, without PSD processing, is also shown here. The unit of Q_{total} is calibrated to MeV, based on the Q_{total} of alpha particles from ^{241}Am as shown in Fig. 7. In the energy deposition spectrum of all pulses in Fig. 9, a dominant peak was found below the deposition energy of 2 MeV, and a smaller peak appeared around 2.7 MeV. The result of the PSD method for gamma-rays indicated that the major part of this spectrum below 2 MeV is likely caused by gamma-rays. The energy deposition spectrum of pulses with wider FWHM showed two peaks, with the peak at higher energy side clearly originating from energetic tritons, assigned from the peak energy. Surprisingly, a peak at lower energy region, which might be caused by alpha particles produced by the ^{6}Li(n,α)^{3}H reaction, could be extracted from many pulses with similar Q_{total} induced by gamma-rays.

These results showed that the energetic triton measurement under gamma-ray irradiation environment were successfully demonstrated using PSD methods.

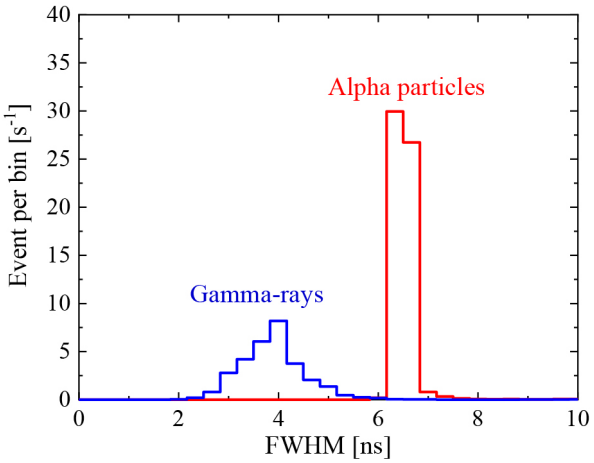

Fig. 6. The FWHM distribution of pulses induced by alpha particles from ~ 550 Bq ^{241}Am and gamma-rays from 0.76 MBq ^{60}Co. The −400 V was applied on the rear surface electrode of the SCD in this measurement. Reproduced with permission from M.I. Kobayashi *et al.* [73].

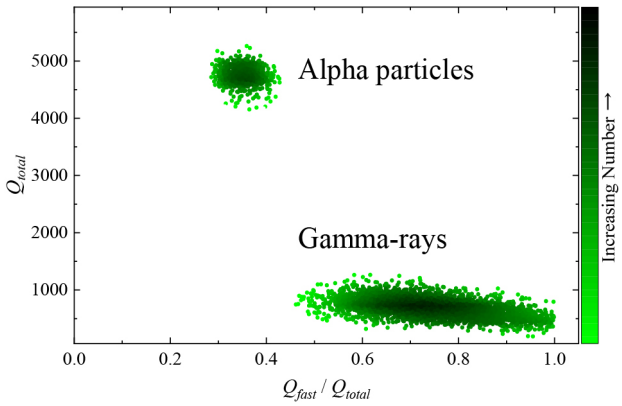

Fig. 7. The result of PSD method using charge-integral for pulses induced by alpha particles from ^{241}Am and gamma-rays from ^{60}Co. The +250 V was applied on the rear surface electrode of the SCD in this measurement. Reproduced with permission from M.I. Kobayashi *et al.* [74].

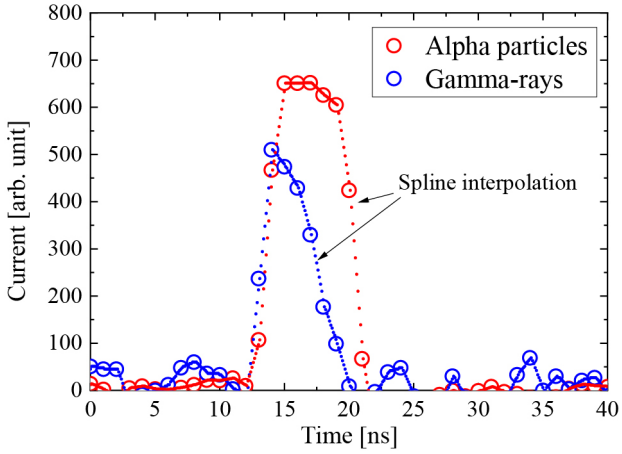

Fig. 8. Typical shape of pulses induced in the SCDD by the irradiation of an alpha particle and a gamma-ray. The −400 V was applied on the rear surface electrode of the SCD in this measurement. Reproduced with permission from M.I. Kobayashi *et al.* [73].

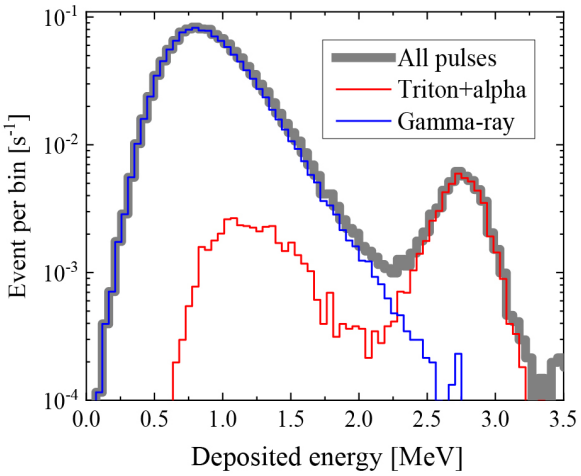

Fig. 9. The energy deposition spectra of the SCDD with ^{6}LiF foil irradiated with decelerated neutrons from a 260 MBq ^{252}Cf source contained in the shielding box. The energy deposition spectra of energetic ions and gamma-rays deduced by the PSD method using pulse width are also displayed. The −400 V was applied on the rear surface electrode of the SCD in this measurement. Reproduced with permission from M.I. Kobayashi *et al.* [73].

3.2 Energetic triton and fast neutron discrimination [75–78]

3.2.1 Estimation of pulse shapes

Although pulses induced by energetic tritons and gamma-rays can be successfully discriminated, fast neutrons are also associated in the BB. Therefore, an effective PSD method should be necessary of discriminating pulses induced by fast neutrons.

Fast neutrons in the SCD induce several nuclear reactions, such as ^{12}C(n,n')^{12}C, ^{12}C(n,n'2α)α, ^{12}C(n,α)^{9}Be, reactions. These reactions produce energetic ions in the SCD. As discussed in Sec. 2.4, these reactions occur randomly at various depths within the SCD, resulting that electron-hole pair distributions that appear as point-like clusters at different depths. As in Sec. 3.1.1, the pulse shapes of the induced current by fast neutrons are estimated based on the equations derived in Sec. 2.3.

Figure 10 summarizes the estimated pulse shapes in the SCDD obtained during fast neutron irradiation. It is assumed that a negative voltage is applied to the incident surface of the SCD, so induced electrons drift toward the rear-side electrode, while induced holes drift toward the incident surface electrode. Fast neutron irradiation can induce several profiles in the SCDD, depending on the depth at which the event occurs.

In the event where a fast neutron hits the incident surface region (near the negative voltage-applied electrode), a rectangular-shaped pulse can be formed as Fig. 10(a). A similar pulse shape can be observed when a fast neutron hits the rear surface of the SCD (see Fig. 10(e)). In these cases, because the charge collection time for either charge (holes for the former, and electrons for the latter) is quite short, the drift of the other charge solely induces the current. Furthermore, the drift velocity of electrons is slower than that of holes in the SCD [35], resulting in a wider rectangular-shaped pulse in Fig. 10(a).

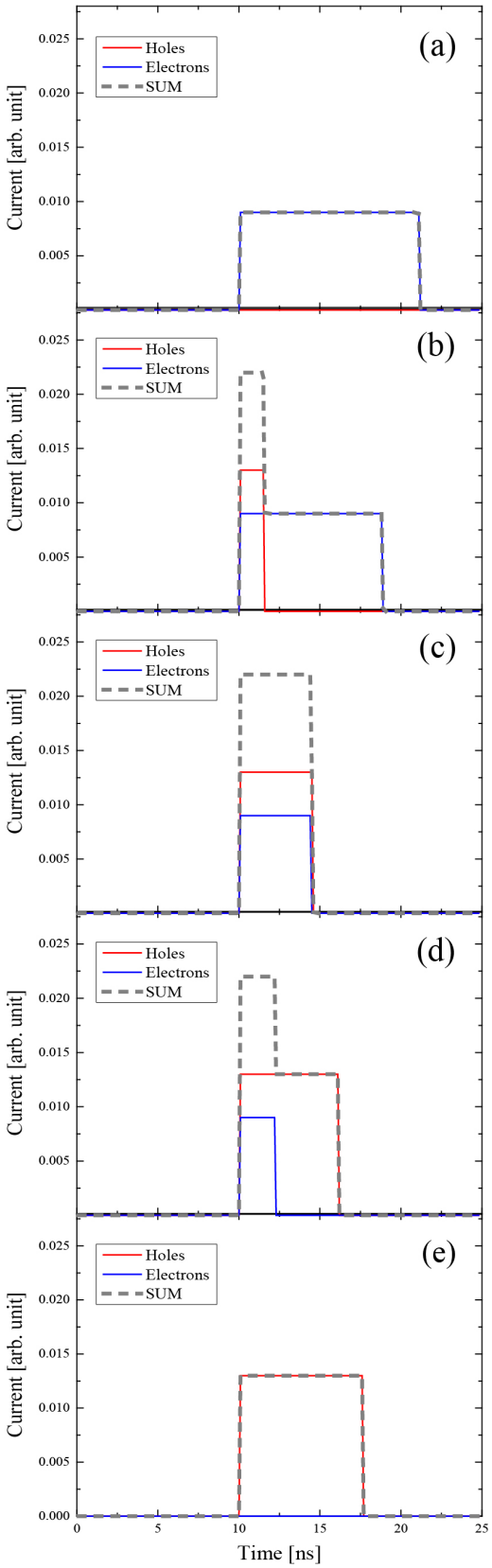

Fig. 10. Predicted waveforms of induced current in the SCDD by irradiation of fast neutron hitting the SCD at (a) near the incident surface, (b) near the depth of 100 μm from the incident surface, (c) at the BCR (near the depth of 300 μm from the incident surface), (d) near the depth of 400 μm from the incident surface, and (e) near the rear surface. The applied voltage of +250 V on the rear surface electrode is assumed.

When a fast neutron hits a different depth region of the SCD, the induced current is a superposition of the drifts of both electrons and holes. Typically, the pulse shape is two-step-like (Figs. 10(b) and (d)), because the charge collection time for one charge differs from that of the other. On the other hand, there is a specific case where the charge collection times for both charges are equivalent. In this event, the resulting pulse shape should be rectangular (see Fig. 10(c)), with the current induced by both electron and hole drift superimposed. However, the pulse width is narrower compared to Figs. 10(a) and (e). This specific depth region of the SCD is known as the Ballistic Center Region (BCR), and the narrow rectangular shaped pulse is indicative of fast neutron events.

The estimation of pulse shapes for fast neutron irradiation of the SCDD indicates that the fast neutron flux can be evaluated by extracting pulses with narrow rectangular shapes. However, detecting energetic tritons may be challenging because fast neutrons can hit the incident surface of the SCD, as is the case with energetic tritons, resulting in a wide rectangular pulse. Therefore, additional analyses are required for wide rectangular shaped pulses to exclude the influence of fast neutrons.

3.2.2 Pulse shape discrimination method based on the rectangularity

Unlike energetic triton irradiation, fast neutron irradiation can induce multiple pulse shapes in the SCDD with varying pulse widths. Therefore, the pulse shape discrimination (PSD) method based solely on pulse width, which is applicable for energetic triton measurement in a gamma-ray irradiation environment, is no longer effective. In this case, an additional parameter is required.

For PSD, a combination of pulse width and the "rectangularity index, *R*" is employed. *R* quantifies how closely the pulse shape resembles a rectangular waveform. It is defined as follows. Given the pulse data for event *j*, after background current subtraction, the waveform is represented as a vector ζ_j, as described in Sec. 3.1.2. First, the time index corresponding to the highest current is identified as $a_{k,j}$ = arg.max(ζ_j). Next, the time indices at one-quarter of the peak height, both before and after the highest current, are determined to evaluate FW1/4PH in the same manner as in Sec. 3.1.2. The rectangularity index R_j is then defined as:

$$R_j = \left(\frac{3a_{k,j}}{4}(\mathrm{FW1/4PH})_j\right)^{-1} \Bigg/ \int_{argmin(\eta_{L,j})}^{argmin(\eta_{R,j})} (a_{i,j} - \delta_j)\,dt \quad . \tag{19}$$

The numerator of this equation represents the integral of the charge exceeding one-fourth of the peak height, while the denominator corresponds to the area of the rectangle formed by FW1/4PH and $3a_{k,j}/4$. When the pulse shape is nearly rectangular, *R* should be close to unity.

Following PSD with *R*, pulses with rectangular shape are further analyzed using pulse width. As discussed in Sec. 3.2.1, three types of events can produce rectangular shaped pulses: fast neutrons hitting both surfaces and the BCR. Consequently, three peaks are expected in the histogram of FW1/4PH. When a negative voltage is applied to the incident surface, narrow rectangular pulses originate from events in the BCR, and rectangular pulses with middle pulse width correspond to events at the rear surface, while wide rectangular pulses correspond to events at the incident surface.

The key advantage of this PSD method is its ability to eliminate pulses induced by gamma-rays. Gamma-rays produce triangular shaped pulses in the SCDD, which can be effectively excluded based on rectangularity. Additionally, pulses induced by fast neutrons can be readily identified as rectangular shaped pulses with narrow pulse widths. Pulses induced by energetic tritons can be measured using rectangular shaped pulses with wide pulse widths, while analyses are necessary to exclude the contribution from fast neutron events.

The demonstration of the PSD method and subsequent analyses for evaluating energetic triton measurements will be presented in the following sections.

3.2.3 Energetic triton measurements under fast neutron irradiation environment

As a demonstration of the capability of the PSD method, the PSD method was applied on the pulses obtained by fast neutron irradiation using D-Li fast neutron source [79]. In this experiment, the SCDD was not equipped with ^{6}LiF foil, ensuring that only fast neutrons contributed to pulse generation. Additionally, a +250 V bias was applied to the rear surface of the SCD within the SCDD. All pulses were analyzed to determine the rectangularity index *R*, and rectangular shaped pulses were extracted and summarized in a histogram based as a function of pulse width. The details of this experiment can be found elsewhere [78].

Figure 11 presents the histogram of rectangular shaped pulses as a function of FW1/4PH in this measurement. For comparison, the FW1/4PH distribution for all pulses is also shown. As predicted in Sec. 3.2.2, three peaks appeared in the histogram. The narrow rectangular shaped pulses were attributed to events occurring at the BCR, while the wide rectangular shaped pulses originated from events at the incident surface. A third peak, corresponding to intermediate-width rectangular shaped pulses, should be associated with events at the rear surface.

Figure 12 displays typical pulse shapes corresponding to these three peaks. In each case, rectangular shaped pulses were observed, and the pulses were clearly distinguished based on pulse width. These results confirm the successful extraction of rectangular shaped pulses with different pulse widths. However, it should be noted that a significant portion of pulses were excluded by the PSD method (Compare the numbers of events of all pulses to rectangular shaped pulses in Fig. 11). This reduction in pulse count leads to a degradation in the statistical accuracy of fast neutron measurements, which is a typical drawback of this approach. Therefore, this limitation should be carefully considered when designing the measurement.

The first method to demonstrate energetic triton measurement under fast neutron irradiation utilizes two SCDDs.

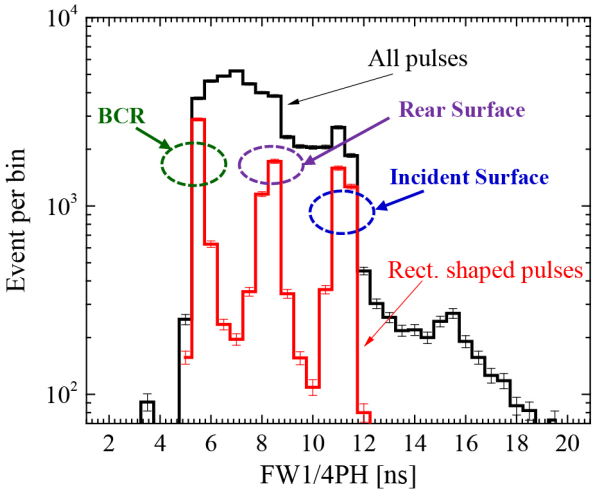

Fig. 11. The FW1/4PH distribution of all pulses and pulses with rectangular shape in the SCDD under fast neutron irradiation in D-Li neutron source at the Fast Neutron Laboratory (FNL) of Tohoku University [79]. Pulses with the deposition energy above 2 MeV are analyzed in this figure. The +250 V was applied on the rear surface electrode of the SCD in this measurement. Reproduced with permission from M.I. Kobayashi *et al.* [78].

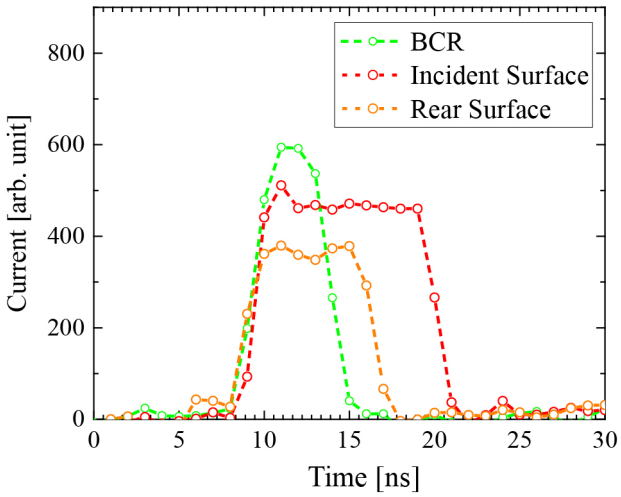

Fig. 12. An example of three types of pulses with a rectangular shape and different pulse widths successfully separated through the PSD method using rectangularity and pulse width. The +250 V was applied on the rear surface electrode of the SCD in this measurement. These pulses with a narrow, a wide, and a middle-wide pulse width are induced by irradiation of fast neutrons hitting at the BCR, the incident surface, and the rear surface, respectively. Reproduced with permission from M.I. Kobayashi *et al.* [78].

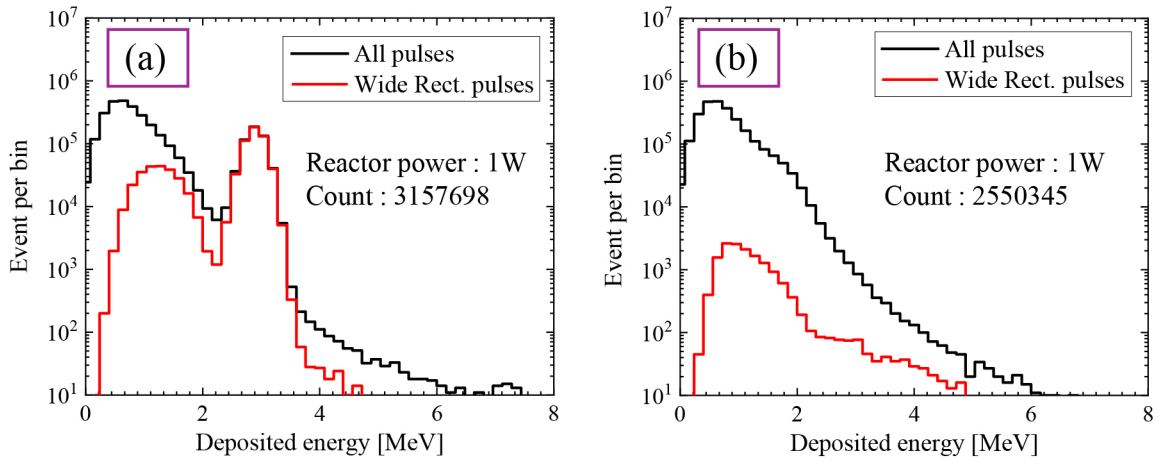

Fig. 13. The energy deposition spectra of all pulses induced in the SCDD (a) with ^{6}LiF foil and (b) without ^{6}LiF foil, installed into the core region of UTR-KINKI. The energy deposition spectra of pulses with a wide rectangular shape are also displayed. The reactor power and total count number are also represented. The +250 V was applied on the rear surface electrode of the SCD in this measurement. Reproduced from M.I. Kobayashi *et al.* [77], with permission from JSPF (the Japan Society of Plasma Science and Nuclear Fusion Research).

One SCDD is equipped with a ^{6}LiF thin foil in front of the SCD, while the other lacks the foil. In this setup, energetic tritons are generated in the detector with the ^{6}LiF foil, and the energy deposition spectrum in the detector without the foil is subtracted to enable the measurement of the energetic triton. An example of this method is shown in Fig. 13, where SCDDs with and without the ^{6}LiF foil were sequentially installed near the reactor core of the UTR-KINKI reactor, which operates at a power of 1 W [80–82]. The irradiation field consists of a broad range of neutron and gamma-ray energies. The dominant neutron energy in the core region is less than 1 eV, although the neutron energy spectrum extends above 5 MeV. The results indicated that the major components of the energy deposition spectrum were concentrated in the lower energy region. This region is likely due to energy deposition events from elastic collisions of fast neutrons and Compton scattering by gamma-rays in the SCD. The results showed clear differences when the ^{6}LiF foil was used. A significant energy deposition around 2.7 MeV was observed in the SCDD with the ^{6}LiF foil. After extracting wide rectangular shaped pulses, a peak near 1.2 MeV was also observed, which may be attributed to alpha particles generated in the ^{6}Li(n,α)^{3}H reaction. Wide rectangular shaped pulses were also observed in the SCDD without the ^{6}LiF foil due to fast neutrons. Therefore,

the energy deposition spectrum of the wide rectangular shaped pulses in the SCDD with the ^{6}LiF foil must be subtracted from the one in the SCDD without the foil, enabling the measurement of energetic tritons in the fast neutron irradiation environment.

While this method is simple and reliable for energetic triton measurements, it requires either two SCDDs in the same position or sequential measurements using a single SCDD with and without the ^{6}LiF foil. Consequently, this method demands additional space in the blanket or more time for measurements in a single plasma operation. To address this limitation, an alternative method is proposed.

The second method for energetic triton measurement under fast neutron irradiation utilizes a single SCDD and effectively applies the results of pulse shape discrimination (PSD). Figure 14 presents the energy deposition spectrum under fast neutron irradiation using a D-Li fast neutron source, comparing the spectra obtained with and without the ^{6}LiF foil. Due to the high maximum neutron energy in the D-Li fast neutron source, the energy deposition spectrum extends up to 14 MeV. The majority of energy deposition events were concentrated in the lower energy region, with additional peaks near 7 and 9.5 MeV due to various nuclear reactions between fast neutrons and the SCD. The assignment of these peaks will be discussed later.

No clear differences were observed in the spectral profiles between the SCDD with and without the ^{6}LiF foil. However, an increase in the event rates of wide rectangular shaped pulses was noted in the SCDD with the ^{6}LiF foil, suggesting additional particle irradiation into the incident surface of the SCD summing with fast neutrons. These additional particles are likely nuclear reaction products generated in the ^{6}LiF foil via neutron interactions. Because of the higher maximum neutron energy in D-Li neutron source, these nuclear reaction products may include not only energetic tritons but also other ions such as energetic protons and alpha particles. However, nuclear data [24, 25] indicate that energetic tritons should be the dominant component. In the following discussion, these nuclear reaction products are regarded as energetic tritons.

This method for energetic triton measurement utilizes both wide and narrow rectangular shaped pulses. First, the ratio of the numbers of wide rectangular shaped pulses to narrow rectangular shaped pulses was evaluated as a function of deposited energy in the SCDD without the ^{6}LiF foil. Since fast neutron interactions occur uniformly throughout the thin SCD, this ratio should be independent of the fast neutron energy distribution. By multiplying this ratio with the number of narrow rectangular shaped pulses in each deposited energy bin for the SCDD with the ^{6}LiF foil, the number of wide rectangular shaped pulses induced solely by fast neutrons in each deposited energy bin can be estimated. Then, subtracting this estimated energy deposition spectrum from the actual energy deposition spectrum of wide rectangular shaped pulses in the SCDD with the ^{6}LiF foil isolates the energy deposition spectrum of energetic tritons. This process is expressed by the following equation:

$$\Psi_i^{ET} = \frac{\Psi_{i,\,with\,LiF\,foil}^{Wide\,Rect.} - \left(\frac{\Psi_{i,\,without\,foil}^{Wide\,Rect.}}{\Psi_{i,\,without\,foil}^{Narrow\,Rect.}} \Psi_{i,\,with\,LiF\,foil}^{Narrow\,Rect.} \right)}{\int \Psi_{i,\,with\,LiF\,foil}^{All} dE}, \quad (20)$$

where Ψ_i in this equation indicates the number of pulses in i-th energy deposition bin to form the energy deposition spectrum. The subscripts in Ψ indicates the abundance of ^{6}LiF foil, while the superscripts in Ψ denote the pulse shapes classification obtained through the PSD method using the rectangularity and pulse width (All refers to all pulses without PSD processing). Ψ_i^{ET} represents the energy deposition spectrum of energetic tritons.

The effectiveness of this method is demonstrated in Fig. 15, which compares the energy deposition spectrum for energetic tritons obtained using this method with that obtained using the first method described earlier in this section. The

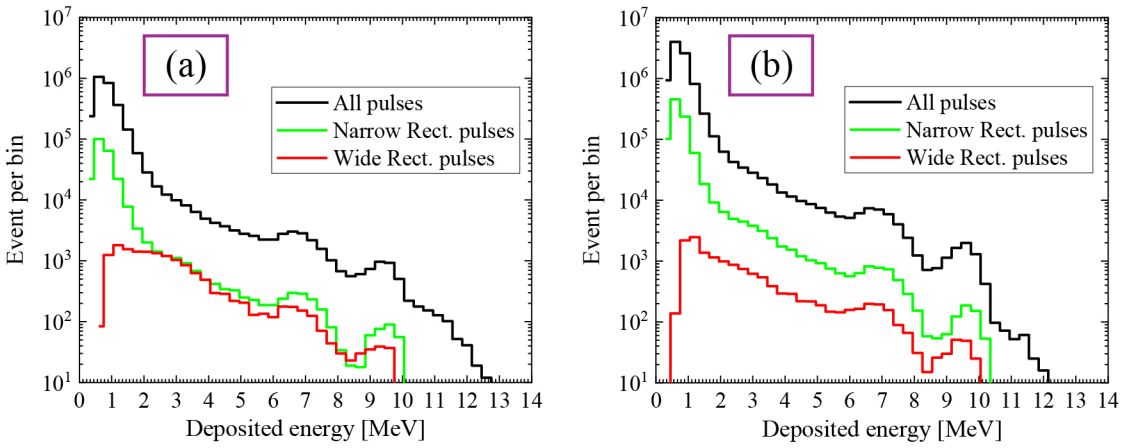

Fig. 14. The energy deposition spectra of all pulses induced in the SCDD (a) with ^{6}LiF foil and (b) without ^{6}LiF foil, under fast neutron irradiation in D-Li neutron source at the FNL of Tohoku University [79]. The energy deposition spectra for pulses with a narrow rectangular shape and a wide rectangular shape are also displayed. The +250 V was applied on the rear surface electrode of the SCD in this measurement. Reproduced with permission from M.I. Kobayashi *et al.* [78].

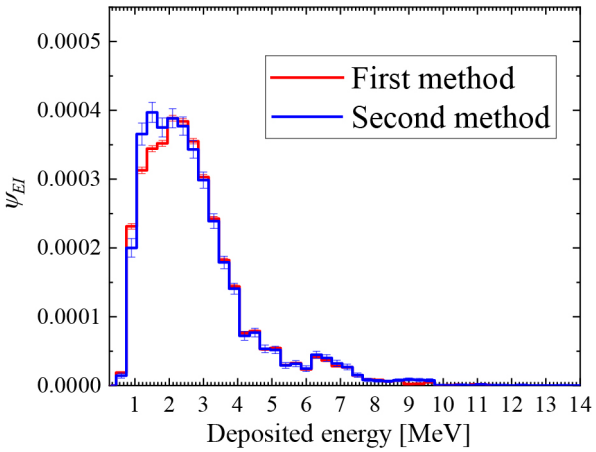

Fig. 15. The deduced energy deposition spectra of energetic tritons in the SCDD with ^{6}LiF foil obtained under fast neutron irradiation in D-Li neutron source at the FNL of Tohoku University [79]. These spectra were deduced by the combination of PSD method and additional analyses using dual SCDD (first method) and a single SCDD (second method) presented in Sec. 3.2.3. Reproduced with permission from M.I. Kobayashi *et al.* [78].

results are remarkably similar, confirming that the second method performs well even with a single SCDD.

3.3 Simultaneous quantification method of the tritium production rate and the fast neutron flux under mixed radiation field

As explained above, the energetic triton measurements are possible under gamma-ray and fast neutron irradiation environments using the PSD method based on rectangularity and pulse width. Additionally, this PSD can extract pulses with a narrow rectangular shape, which are exclusively induced by fast neutrons. Consequently, pulses induced by energetic tritons and fast neutrons can be simultaneously obtained through the PSD method.

In this section, we present the conversion method from the results of PSD methods to the tritium production rate and the fast neutron flux, which are the key engineering parameters of BB. In conclusion, simultaneous measurements of the tritium production rate and the fast neutron flux under mixed radiation field using the SCDD are comprehensively demonstrated.

3.3.1 The evaluation of tritium production rate [83]

As discussed in Sec. 2.4, most energetic tritons that reach the SCD deposit their entire energy in the surface region of the SCD. Also, thanks to very low impurity level in the detector-grade SCD, the charge collection efficiency can reach to 100%. Therefore, the conversion of energetic triton measurement results into a tritium production rate requires the evaluation of two factors:

1. The energy loss of bred tritons in the ^{6}LiF foil.
2. The transport efficiency of energetic tritons from the foil to the SCD.

These factors can be assessed through particle transport calculations. Here, we use PHITS for this evaluation.

Since energetic tritons are charged particles, their energy loss process in the ^{6}LiF foil significantly influences subsequent energy deposition in the SCD. The energy loss of energetic tritons depends on the thickness of the ^{6}LiF foil. Therefore, the energy of tritons produced by the ^{6}Li(n,α)^{3}H reaction and subsequently emitted from the ^{6}LiF foil was estimated. Figure 16 shows the energy spectrum of energetic ions emitted from the ^{6}LiF foil, as evaluated by PHITS. Two foil thicknesses were considered: 1.9 and 350 μm. In this calculation, thermal neutrons were uniformly distributed within the foil, and the transport of generated energetic ions was analyzed. For the 1.9 μm-thick foil, two peaks were observed, corresponding to energetic alpha particles and tritons generated via the ^{6}Li(n,α)^{3}H reaction. The peak position of tritons was approximately 2.7 MeV, which aligns with the expected kinetic energy of tritons produced in thermal neutron irradiation. The alpha particle peak appeared from around 2.0 MeV, as estimated from the Q-value of the ^{6}Li(n,α) ^{3}H reaction. Alpha particles with lower energies were observed, suggesting energy loss of alpha particles within the ^{6}LiF foil.

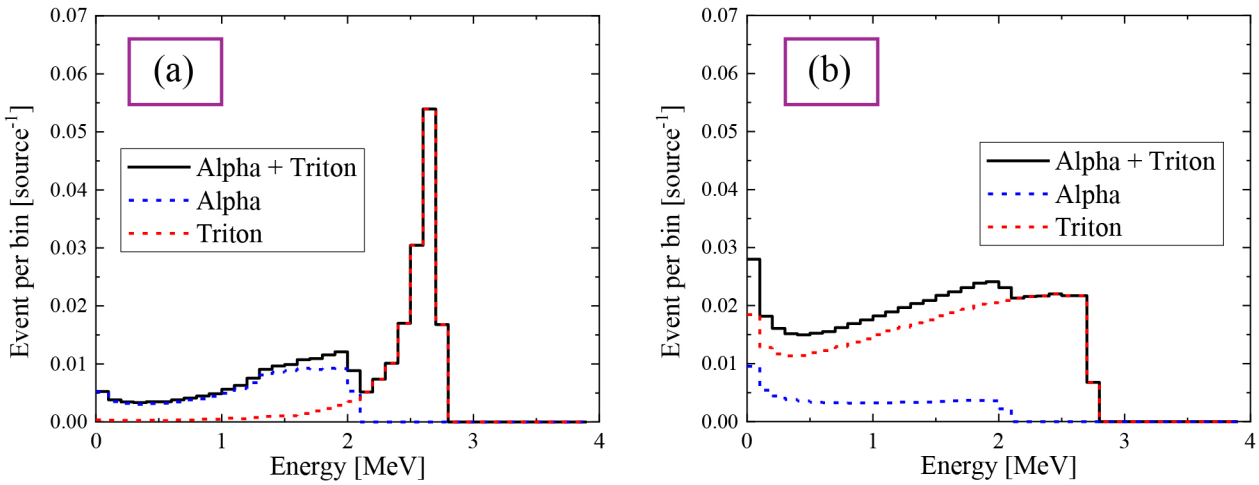

Fig. 16. Energy distribution of emitted triton and alpha particles from (a) 1.9 μm-thick ^{6}LiF foil and (b) 350 μm-thick ^{6}LiF foil estimated by the T-track tally of PHITS code. These energetic ions are generated through the ^{6}Li(n,α)^{3}H reaction occurred uniformly in the ^{6}LiF foil by thermal neutrons.

The results for the 350 μm-thick foil were markedly different. A broad peak was observed, indicating substantial energy loss of energetic particles. The total event for the 350 μm-thick ^{6}LiF foil was approximately 2.5 times higher than that for the 1.9 μm-thick foil. This result implies that the emission rate of energetic ions would be higher for the 350 μm-thick LiF foil. However, quantifying the number of energetic tritons in this case would be challenging due to energy broadening into the lower energy region. In particular, pulses with lower deposition energy are more likely to be rejected by the threshold current of the DAQ system, which is set to filter out noise. As a result, accurately quantifying energetic triton events becomes difficult. Therefore, a 1.9 μm-thick ^{6}LiF foil is the more suitable choice for quantifying the tritium production rate.

The transport efficiency of energetic tritons depends solely on the geometric orientation of the ^{6}LiF foil, the SCD, and the housing of the SCDD. As an example, Fig. 17 illustrates a typical transport behavior of energetic tritons emitted from the ^{6}LiF foil into the SCD. The thickness of ^{6}LiF foil is 1.9 μm. In this setup, the SCDD is housed in a polyether ether ketone (PEEK) casing. The SCD is positioned inside the housing and faces the ^{6}LiF foil through an air gap with a diameter of 3.6 mm and a thickness of 1.1 mm. The results show a concentric distribution of energetic tritons, which arises due to the radially uniform emission of tritons from the foil and the stopping of some tritons by the housing.

The detection efficiency of energetic tritons represents the transport probability of bred tritons emitted from the ^{6}LiF foil into the SCD. Our previous study indicated that approximately 18% of the energetic tritons generated in the foil can reach and deposit their energy into the SCD under the same configuration as in Fig. 17. This result was consistent with actual measurements [74].

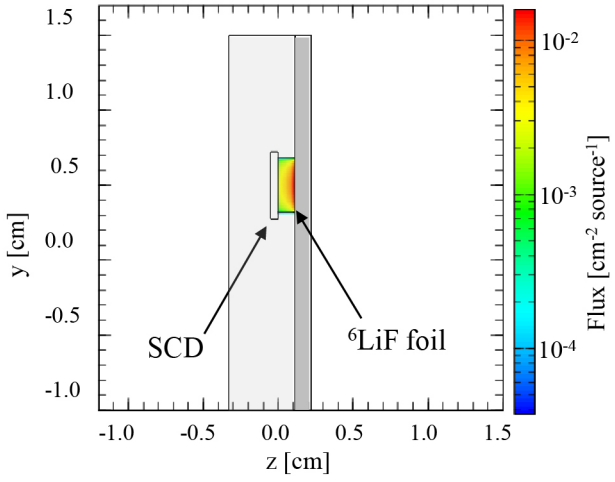

Fig. 17. The transport behaviors of energetic tritons generated through the ^{6}Li(n,α)^{3}H reaction in the 1.9 μm-thick ^{6}LiF foil under thermal neutron irradiation estimated by the T-track tally of PHITS code. The SCDD in this calculation is a B-6 high-temperature thermal neutron detector [64] colored with gray. The color map represents the flux distribution of energetic tritons. Reproduced with permission from M.I. Kobayashi *et al.* [74].

3.3.2 The evaluation of fast neutron flux [84, 85]

Fast neutrons induce various nuclear reactions inside the SCD, and nuclear reaction products generated through these reactions deposit energy into the SCD, making them detectable. Some of these events can be measured as pulses with a narrow rectangular shape, which can be extracted by the PSD method. Therefore, precise reaction cross-sections of nuclear reactions are necessary to evaluate the fast neutron flux. Additionally, as explained in Sec. 3.2.3, a significant portion of pulses induced by fast neutrons is lost during the PSD processes. Thus, these lost portions must be accounted for in the evaluation.

The evaluation of the radiation flux from the detector responses is an inverse problem analysis, and various methods have been developed [86–90]. In this study, we applied the response matrix method [91–93]. The energy deposition spectrum of pulses with narrow rectangular shape $\Psi_i^{Narrow\ Rect}$, can be expressed as follows.

$$\Psi_i^{Narrow\ Rect.} = \frac{\omega_i}{\theta} \sum_{j=1}^{N} P_{i,j} \phi_j t \,. \tag{21}$$

Here, ω, θ, P, ϕ, and t represent the noise-cut function, the overall PSD efficiency correction factor, the response matrix of the SCD for neutrons, the number of incident neutrons into the SCD in unit time, and the irradiation duration, respectively. The subscript i indicates the deposition energy bin number, while the subscript j denotes the index number of fast neutron energy in the response matrix. The overall PSD efficiency correction factor is required because narrow rectangular shaped pulses are only a subset of fast neutron induced pulses.

The response matrix $\boldsymbol{P}$ is structured as follows.

$$\boldsymbol{P} = \begin{bmatrix} P_{1,1} & P_{1,2} & \cdots & P_{1,j} & \cdots & P_{1,M-1} & P_{1,M} \\ P_{2,1} & P_{2,2} & & \vdots & & P_{2,M-1} & P_{2,M} \\ \vdots & & \ddots & & \ddots & & \vdots \\ P_{i,1} & \cdots & & P_{i,j} & & \cdots & P_{i,M} \\ \vdots & & \ddots & & \ddots & & \vdots \\ P_{N-1,1} & P_{N-1,2} & & \vdots & & P_{N-1,M-1} & P_{N-1,M} \\ P_{N,1} & P_{N,2} & \cdots & P_{N,j} & \cdots & P_{N,M-1} & P_{N,M} \end{bmatrix}. \tag{22}$$

$P_{i,j}$ indicates the energy deposition efficiency of the SCD at the i-th deposition energy bin by a neutron in the j-th energy bin. This response matrix can be obtained through radiation transport calculations, which evaluate the energy deposition efficiency of the SCD across all energy bins by varying the energy of incident neutrons. Several specific models for nuclear reactions of carbon atoms with fast neutrons are available in Geant4 for precise evaluation of the response matrix for the SCDD [94, 95].

The overall PSD efficiency is determined by the ratio of counts of narrow rectangular shaped pulses to counts of all pulses. The noise-cut function modifies the response matrix to account for the effects of the current threshold in DAQ system, which is set for noise suppression. The details on this function can be found elsewhere [84].

The fast neutron flux can then be deduced by minimizing

the residual f, through an iterative process that updates ϕ in each iteration step:

$$f_i = \Psi_i^{Narrow\ Rect.} - \frac{\omega_i}{\theta}\sum_{j=1}^{M} P_{i,j}\phi_j t, \tag{23}$$

$$\boldsymbol{\phi}^{(l+1)} = \boldsymbol{\phi}^{(l)} - \left[\frac{\partial \boldsymbol{f}}{\partial \boldsymbol{\phi}}\right]^{-1}\boldsymbol{f}, \tag{24}$$

where the superscript (l) indicates the iteration step number. The iterative calculation terminates when the following convergence condition is met in all energy bins.

$$\left|\frac{\boldsymbol{\phi}^{(l+1)} - \boldsymbol{\phi}^{(l)}}{\boldsymbol{\phi}^{(l)}}\right| = 10^{-10}. \tag{25}$$

Figure 18 illustrates the fast neuron flux evaluation using the present method. In these experiments, mono-energetic neutrons of 14.1 and 5.5 MeV were irradiated into the SCDD without a ^{6}LiF foil [96]. The PSD method, using rectangularity and pulse width, was applied to separately count pulses with a narrow rectangular shape, and evaluate the energy deposition spectrum as shown in Figs. 18(a) and (c). In the case of 14.1 MeV neutron irradiation, multiple energy deposition peaks appear, similar to those in Fig. 14, due to various nuclear reactions between fast neutrons and carbon atoms. According to previous studies, peaks around 8.4, 6 and 3 MeV correspond to energy deposition events of energetic ions produced by ^{12}C(n,α)^{9}Be (Q ~ −5.702 MeV), ^{12}C(n,n'2α)α (Q ~ −7.275 MeV) and ^{12}C(n,n')^{12}C (Q ~ 0 MeV) reactions, respectively [34, 97]. For the case of 5.5 MeV neutron irradiation, a single energy deposition peak appeared around 1 MeV. The 5.5 MeV neutrons lack sufficient energy to induce nuclear reactions such as ^{12}C(n,α)^{9}Be reaction, accordingly only elastic collision processes would contribute to this peak.

Figures 18(b) and (d) show the neutron energy spectrum ϕt deduced using the response matrix method. The energy

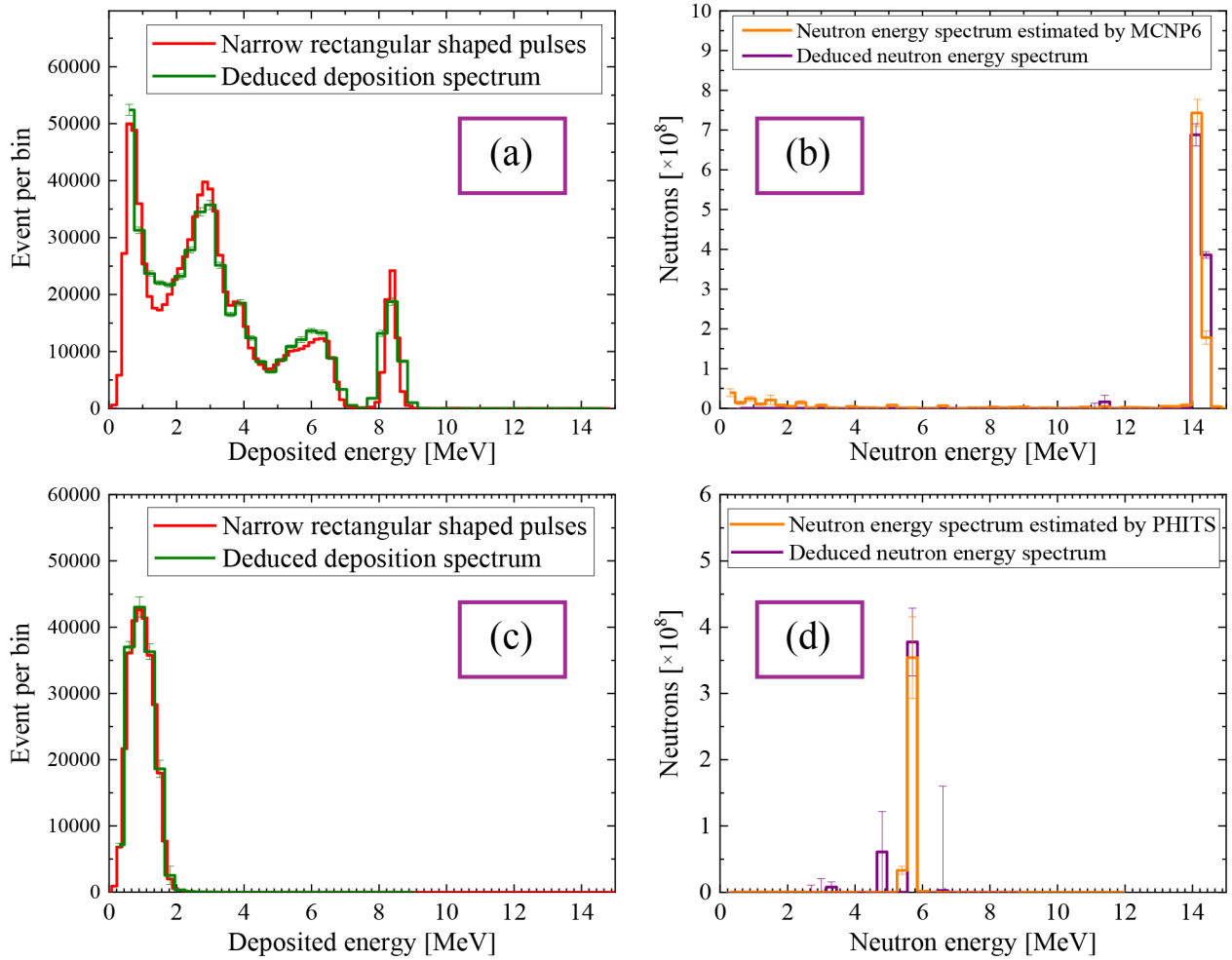

Fig. 18. The results of neutron energy spectrum evaluation. (a) The comparison between the energy deposition spectrum of narrow rectangular shaped pulses obtained by the PSD method and the estimated deposition spectrum in 14.1 MeV neutron irradiation experiment at OKTAVIAN of Osaka University [96], (b) the comparison between the deduced neutron energy spectrum by the response matrix method and the neutron energy spectrum estimated by MCNP6. The respective results are displayed in (c) and (d) for 5.5 MeV neutron irradiation experiment at the FNL of Tohoku University [79] and estimated by PHITS code. The +250 V was applied on the rear surface electrode of the SCD in this measurement. The overall PSD efficiency correction factor is the reciprocal of 0.135 ± 0.04 from the results of 14.1 MeV neutron irradiation experiment. Reproduced with permission from M.I. Kobayashi *et al.* [84].

deposition spectrum of pulses with a narrow rectangular shape deduced from these evaluated neutron energy spectrum are also plotted in Figs. 18(a) and (c). The neutron energy spectra in these irradiation experiments were estimated using radiation transport calculations performed with the Monte Carlo N-Particle code (MCNP6) and PHITS, and the results are displayed in Figs. 18(b) and (d). Regarding the energy deposition spectrum, the actual and estimated deposition spectra are quantitatively similar, with minor discrepancies likely caused by limitations in nuclear data libraries. In the neutron energy spectra, the estimated mono-energetic neutron flux in both cases, as obtained using the response matrix method, is quantitatively consistent with the radiation transport calculations. These results indicate a successful evaluation of fast neutron flux using the SCDD in combination with the PSD method and the response matrix method.

3.3.3 A comprehensive demonstration of the simultaneous measurements of tritium production rate and fast neutron flux under a mixed radiation field

In the comprehensive demonstration experiments, a neutron irradiation field containing thermal neutrons, 14 MeV neutrons, and gamma rays was required. To achieve this, a neutron moderator was used. The SCDD equipped with a ^{6}LiF foil was placed inside a cylindrical neutron moderator made of polyethylene, which effectively slows down neutrons while minimizing neutron capture probability. The 14.1 MeV neutrons from the neutron source were decelerated within the moderator, resulting in the SCDD being irradiated with both 14.1 MeV neutrons and thermally decelerated neutrons. Additionally, some neutrons were eventually captured by the moderator and various components in the irradiation room, leading to the emission of gamma-rays, which also irradiated the SCDD. Therefore, this setup successfully created a mixed radiation field. The details of this experiment can be found elsewhere [85].

Pulses obtained in the SCDD were analyzed using the PSD method based on rectangularity and pulse width. The resulting energy deposition spectra are shown in Fig. 19. The figure displays the energy deposition spectra for all pulses, as well as for narrow rectangular shaped pulses and wide rectangular shaped pulses, both of which were simultaneously extracted using the PSD method. Compared to Fig. 18(a), which shows the energy deposition spectrum for an SCDD without a ^{6}LiF foil irradiated with 14.1 MeV neutrons, the energy deposition spectrum for all pulses in this experiment was concentrated in the lower energy region. However, a significant peak at 2.7 MeV, corresponding to energetic tritons, was observed. The increased signal in the lower energy region is likely due to contributions from scattered neutrons and gamma-rays. The presence of a distinct peak for energetic tritons confirms that low energy neutrons were effectively produced by the neutron moderator.

The energy deposition spectrum for pulses with a wide rectangular shape is separately displayed in Fig. 20(a). The spectrum exhibits a prominent peak at 2.7 MeV, along with various peaks extending up to 8.4 MeV. In particular, the

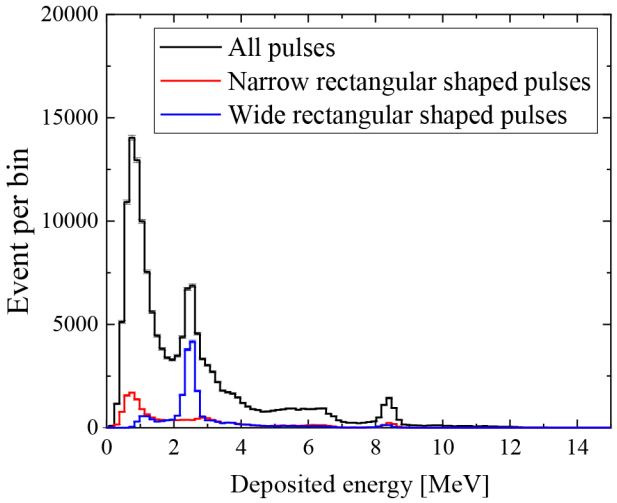

Fig. 19. The energy deposition spectra of all pulses, narrow rectangular shaped pulses, and wide rectangular shaped pulses. The SCDD with the 1.9 μm-thick ^{6}LiF foil was installed in a neutron moderator and irradiated with 14.1 MeV neutrons at OKTAVIAN of Osaka University [96]. The +250 V was applied on the rear surface electrode of the SCD in this measurement. Reproduced with permission from M.I. Kobayashi *et al.* [85].

8.4 MeV peak serves as evidence of the of ^{12}C(n,α)^{9}Be reaction occurring at the incident surface of the SCD. To subtract pulses induced by fast neutrons, the method described in Eq. (20) was applied. The resulting energy deposition spectrum, excluding contributions from fast neutrons, is shown in Fig. 20(b). The energy deposition above 3 MeV was completely removed. In addition to the peak corresponding to energetic tritons, a small peak around 1 MeV was observed, which may be attributed to alpha particles generated in the ^{6}Li(n,α)^{3}H reaction. The number of energetic tritons injected into the SCD was obtained by integrating the energy deposition spectrum in Fig. 20(b) over the energy range of 2–3 MeV. Then, dividing this number by the transport probability of energetic tritons from the ^{6}LiF foil to the SCD allowed for the determination of the tritium production rate in the foil. The measured tritium production rate was found to be consistent with radiation transport calculations [85], confirming the successful evaluation of the tritium production rate using the PSD method and additional analysis.

The energy deposition spectrum for narrow rectangular shaped pulses is exclusively displayed in Fig. 21(a). The spectral profile closely resembles that of the spectrum before PSD processing in Fig. 19, except for the absence of the energetic triton peak. As in Sec. 3.3.2, the neutron energy spectrum was deduced from the energy deposition spectrum using the response matrix method, and the results are shown in Fig. 21(b). Additionally, the energy deposition spectrum obtained by calculating the right-hand side of Eq. (21) using the deduced neutron energy spectrum is included in Fig. 21(a). The actual and deduced energy deposition spectra were in close agreement. The neutron energy spectrum was also consistent with radiation transport calculations in the energy region around 14 MeV, demonstrating the successful evaluation of

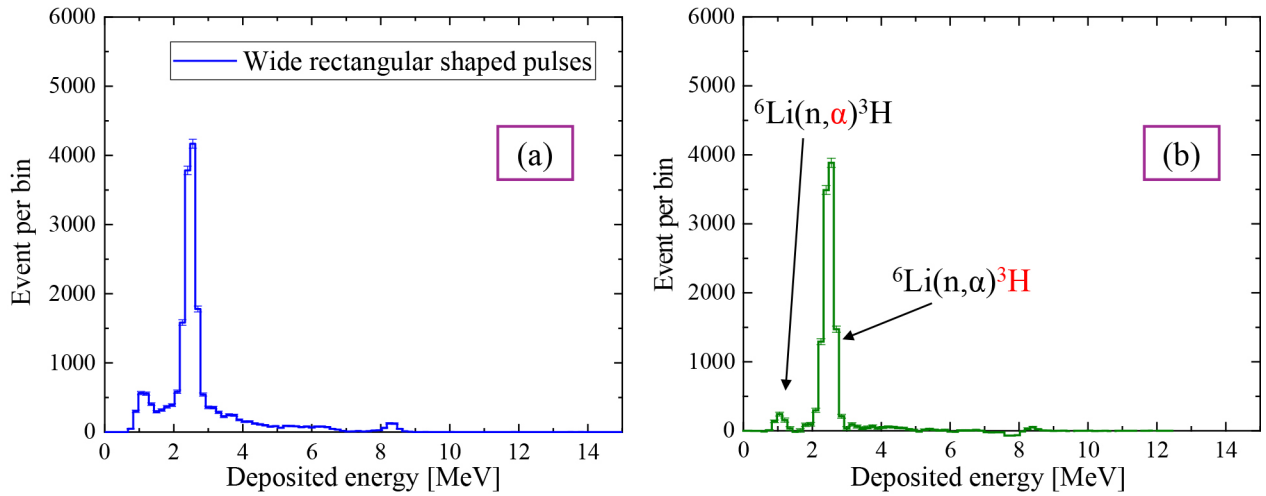

Fig. 20. (a) The energy deposition spectrum of wide rectangular shaped pulses obtained under 14.1 MeV neutron irradiation into the SCDD with 1.9 μm-thick ^{6}LiF foil installed in a neutron moderator, and (b) the deduced energy deposition spectrum of energetic ions in this experiment. The +250 V was applied on the rear surface electrode of the SCD in this measurement. Reproduced with permission from M.I. Kobayashi *et al.* [85].

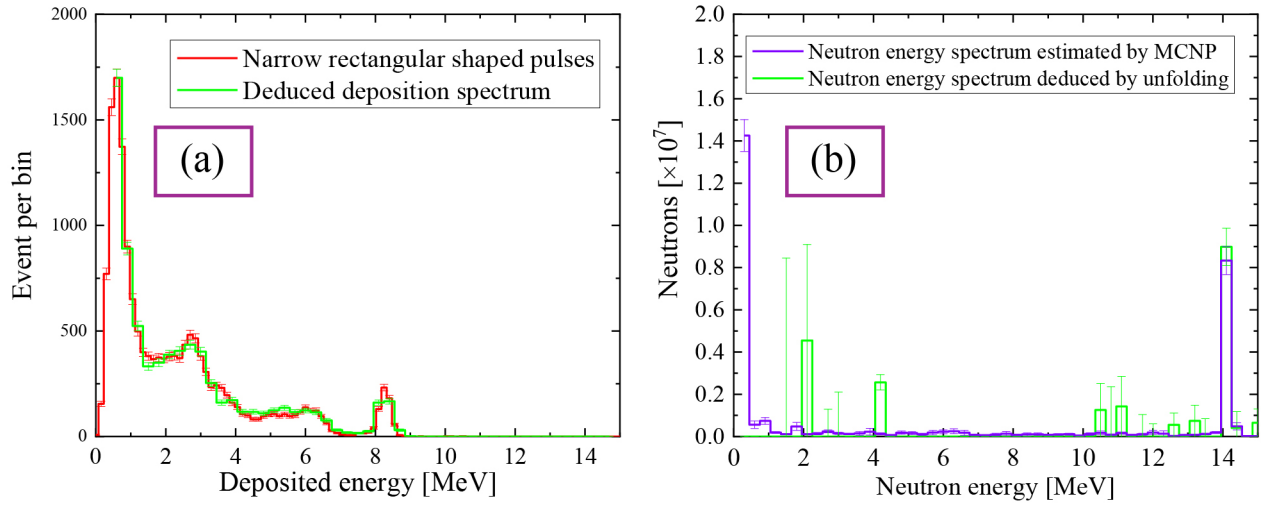

Fig. 21. (a) The energy deposition spectrum of narrow rectangular shaped pulses obtained under 14.1 MeV neutron irradiation into the SCDD with 1.9 μm-thick ^{6}LiF foil installed in a neutron moderator, with the comparison to the deduced energy deposition spectrum with Eq. (21), and (b) the deduced neutron energy spectrum by the response matrix method with the comparison of the results in the neutron transport calculation using MCNP6.

fast neutron flux using this method. However, the neutron flux below 1 MeV was inconsistent with radiation transport calculations. This discrepancy arises because the SCDD itself has limited sensitivity to low energy neutrons. Nevertheless, neutron flux in this lower energy region can still be inferred from the tritium production rate measurement described above.

4. Conclusion and Future Work

In this study, we comprehensively introduced the single-crystal diamond-based detector (SCDD) and its radiation detection process. Based on the detection mechanisms of the SCDD, several pulse shape discrimination (PSD) methods applicable to the performance evaluation of the breeding blanket (BB) were proposed. Building upon these principles, we developed the simultaneous evaluation method of the tritium production rate and the fast neutron flux in a mixed radiation field using only a single SCDD.

In performance testing of the BB, it is essential to measure both the tritium production rate and the fast neutron flux in a mixed radiation field where intense gamma radiation is present. Detectors employed in such environments must therefore exhibit long-term stability, high radiation hardness, and tolerance to temperature variations. In addition, they should minimize perturbations to the local radiation field caused by the presence of the detector itself. Conventional neutron detectors such as fission chambers, ^{3}He counters, ^{6}Li-glass scintillators, and organic scintillators do not fully satisfy these technical requirements due to limitations in size, radiation tolerance, temperature dependence, and gamma discrimination capability. In contrast, the SCDD satisfies all these requirements owing to its compact geometry, excellent radiation hardness, high-temperature operability, and superior energy resolution. Building upon these intrinsic properties,

the simultaneous measurement method for the tritium production rate and fast neutron flux developed in this study demonstrates the extended capability of the SCDD for BB performance evaluation under fusion-relevant conditions.

Before concluding, we highlight some future challenges for the SCDD.

1. Application in Harsh Environments
   Some studies have reported that detection efficiency degrades under intense radiation and high-temperature conditions [98, 99]. Establishing a robust radiation discrimination method in such environments is a critical challenge. We aim to develop improved methods based on the findings of this study.
2. Expanding the Application Field of the SCDD
   As shown in Fig. 11, the PSD method using rectangularity and pulse width can distinguish three types of rectangular shaped pulses with different pulse widths. In this study, we utilized narrow rectangular shaped pulses for fast neutron measurement and wide rectangular shaped pulses for energetic triton measurement. However, middle-wide rectangular shaped pulses, induced at the rear surface region of the SCD in Fig. 11, were also distinguishable but not utilized. These pulse events could provide additional specific radiation measurements.
   For instance, a thin foil containing ^{7}Li can produce energetic ions through nuclear reactions with fast neutrons. By modifying the SCDD structure used in this study to include a thin ^{7}Li foil on the rear surface of the SCD, it may be possible to measure the ^{7}Li burn-up rate in addition to fast neutron flux and tritium production rate. The ^{7}Li burn-up rate measurement would be particularly valuable for BB development using liquid lithium, where tritium production via ^{7}Li burn-up is significant [100]. Therefore, further development and testing of the SCDD with this modified structure will be conducted to enable advanced measurements.

Acknowledgements

This work is supported by the NINS program for cross-disciplinary study (Grant number 0131190). This work is also performed with the support and under the auspices of the NIFS Collaboration Research program (NIFS19KOAA001, NIFS19KLPA001), and LHD project budget.

[1] IAEA Bulletin, 2021, https://www.iaea.org/bulletin/62-2.
[2] S. Meschini *et al.*, Front. Energy Res. **7**, 1157394 (2023).
[3] C.L. Smith and S. Cowley, Phil. Trans. R. Soc. A **368**, 1091 (2010).
[4] K. Hesch *et al.*, WPBB-PR (18) 20555, (2018).
[5] M. Abdou *et al.*, Fusion Eng. Des. **100**, 2 (2015).
[6] F. Dobran, Prog. Nucl. Energy **60**, 89 (2012).
[7] M.D. Anderton *et al.*, Fusion Eng. Des. **210**, 114732 (2025).
[8] L.V. Boccaccini and C. Day, *Encyclopedia of Nuclear Energy*, (Elsevier, 2021), p. 620.
[9] S. Zheng and T.N. Todd, Fusion Eng. Des. **98–99**, 1915 (2015).
[10] Y. Lee *et al.*, Fusion Eng. Des. **205**, 114561 (2024).
[11] Q. Ling and G. Wang, Annals. Nucl. Energy **145**, 107541 (2020).
[12] T. Muroga *et al.*, Fusion Eng. Des. **61–62**, 13 (2002).
[13] Y. Kawamura *et al.*, Fusion Eng. Des. **201**, 114260 (2024).
[14] A. Someya *et al.*, Fusion Eng. Des. **98–99**, 1872 (2015).
[15] S. Liu *et al.*, Fusion Eng. Des. **177**, 113059 (2022).
[16] X. Wu *et al.*, Fusion Eng. Des. **173**, 112797 (2021).
[17] L. Giancarli *et al.*, Fusion Eng. Des. **158**, 111674 (2020).
[18] G. Federici *et al.*, Fusion Eng. Des. **141**, 30 (2019).
[19] J. Miyazawa *et al.*, Fusion Eng. Des. **136**, 1278 (2018).
[20] R. Pearson *et al.*, IEEE Trans. Plasma Sci. **50**, 4406 (2022).
[21] D.B. Pelowits, MCNP6 User's Manual, Los Alamos National Laboratory Tech. Rep. LA-CP-13-00634, Los Alamos National Laboratory, (2013).
[22] T. Sato *et al.*, J. Nucl. Sci. Technol. **55**, 684 (2018).
[23] S. Agostinelli *et al.*, Nucl. Instrum. Meth. A **506**, 250 (2003).
[24] ENDF/B-VII.1 Evaluated Nuclear Data Library, Brookhaven National Laboratory, https://www.nndc.bnl.gov/endf-b7.1/.
[25] G. Chiba *et al.*, J. Nucl. Sci. Technol. **48**, 172 (2011).
[26] G.S. Was *et al.*, J. Nucl. Mater. **527**, 151837 (2019).
[27] C. Cabet *et al.*, J. Nucl. Mater. **523**, 510 (2019).
[28] S. Koizumi *et al.*, *Physics and Applications of CVD Diamond*, (Wiley-VCH Verlag GmbH & Co. KGaA, 2008).
[29] C.E. Nebel, Semicond. Sci. Technol. **18**, S1 (2003).
[30] U.F. Ahmad *et al.*, Mater. Today Commun. **36**, 106409 (2023).
[31] M. Schwander and K. Partes, Diam. Relat. Mater. **20**, 1287 (2011).
[32] https://cividec.at.
[33] E. Griesmayer and B. Dehning, Phys. Procedia **37**, 1997 (2012).
[34] M. Angelone and C. Verona, J. Nucl. Eng. **2**, 422 (2021).
[35] C. Weiss, *PhD thesis*, (Technische Universität Wien, Faculty of Physics, Vienna, 2014).
[36] M. Cerv, *PhD thesis*, (Technische Universität Wien, Faculty of Physics, Vienna, 2016).
[37] S. Sze and K. Kwok, *Physics of Semiconductor Devices 3rd ed.*, (Wiley-Interscience, 2006).
[38] J. Koike *et al.*, Appl. Phys. Lett. **60**, 1450 (1992).
[39] M. Jung *et al.*, Nucl. Instrum. Meth. A **511**, 417 (2003).
[40] S. Liu *et al.*, Nucl. Instrum. Methods Phys. Res. **832**, 231 (2016).
[41] H. Jansen *et al.*, J. Instrum. **8**, P01017 (2013).
[42] H. Jansen *et al.*, *PhD Thesis*, (Rheinische Friedrich-Wilhelms-Universität Bonn, 2013).
[43] M. Sasao *et al.*, Fusion Sci. Technol. **53**, 604 (2008).
[44] M. Isobe *et al.*, Rev. Sci. Instrum. **72**, 611 (2001).
[45] T. Saida *et al.*, Nucl. Fusion **44**, 488 (2004).
[46] M. Ishikawa *et al.*, Plasma Fusion Res. **2**, 019 (2007).
[47] C. Cazzaniga *et al.*, Rev. Sci. Instrum. **85**, 043506 (2014).
[48] B. Caiffi *et al.*, IEEE Trans. Nucl. Sci. **63**, 2409 (2016).
[49] J.H. Kaneko *et al.*, Rev. Sci. Instrum. **75**, 3581 (2004).
[50] M. Angelone *et al.*, Nucl. Instrum. Meth. A **595**, 616 (2008).
[51] M. Isobe *et al.*, Fusion Eng. Des. **34–35**, 573 (1997).
[52] C. Cazzaniga *et al.*, Rev. Sci. Instrum. **85**, 043506 (2014).
[53] B. Caiffi *et al.*, IEEE Trans. Nucl. Sci. **63**, 2409 (2016).
[54] A.V. Krasilnikov *et al.*, Rev. Sci. Instrum. **68**, 553 (1997).
[55] V.D. Kovalchuk *et al.*, Nucl. Instrum. Meth. A **351**, 590 (1994).
[56] K. Ogawa *et al.*, J. Instrum. **18**, P01022 (2023).
[57] M. Angelone *et al.*, Rad. Meas. **46**, 1686 (2011).
[58] M. Marinelli *et al.*, Appl. Phys. Lett. **89**, 143509 (2006).
[59] M. Pillon *et al.*, IEEE Trans. Nucl. Sci. **58**, 1141 (2011).
[60] M. Angelone *et al.*, Fusion Eng. Des. **146**, 1755 (2019).
[61] P. Kavrigin *et al.*, Nucl. Instrum. Methods Phys. Res. A **795**, 88 (2015).
[62] C. Weiss *et al.*, Phys. J. A **52**, 269 (2016).
[63] https://cividec.at/index.php?module=public.product&idProduct=

26&scr=0.
[64] https://cividec.at/index.php?module=public.product&idProduct=18&scr=0.
[65] S. Kamio *et al.*, Rev. Sci. Instrum. **91**, 113304 (2020).
[66] K. Ogawa *et al.*, Rev. Sci. Instrum. **89**, 113509 (2018).
[67] G.F. Knoll, *Radiation Detection and Measurement, 4th ed.*, (John Wiley & Sons Inc., 2010).
[68] W. Shockley, J. Appl. Phys. **9**, 635 (1938).
[69] Z. He, Nucl. Instrum. Methods Phys. Res. A **463**, 250 (2001).
[70] Database for Prompt Gamma-ray Neutron Activation Analysis, https://www-nds.iaea.org/pgaa/.
[71] D.G. Cacuci ed., *Handbook of Nuclear Engineering Vol. 1: Nuclear Engineering Fundamentals*, (Springer, 2010).
[72] S.P. Chabod, Nucl. Instrum. Methods Phys. Res. A **669**, 32 (2012).
[73] M.I. Kobayashi *et al.*, Fusion Eng. Des. **161**, 112063 (2020).
[74] M.I. Kobayashi *et al.*, Fusion Eng. Des. **179**, 113117 (2022).
[75] C. Weiss *et al.*, Eur. Phys. J. A **52**, 269 (2016).
[76] P. Kavrigin *et al.*, Eur. Phys. J. A **52**, 179 (2016).
[77] M.I. Kobayashi *et al.*, Plasma Fusion Res. **17**, 2405045 (2022).
[78] M.I. Kobayashi *et al.*, Fusion Eng. Des. **193**, 113799 (2023).
[79] S. Matsuyama *et al.*, Nucl. Instrum. Meth. Phys. Res. B **318A**, 32 (2014).
[80] UTR-KINKI research reactor of the KINDAI University, Japan https://www.kindai.ac.jp/files/rd/research-center/aeri/guide/external-use/outside4.pdf (in Japanese).
[81] S. Endo *et al.*, Appl. Rad. Isotopes **124**, 90 (2017).
[82] S. Endo *et al.*, Appl. Rad. Isotopes **65**, 1037 (2007).
[83] M. Kobayashi *et al.*, J. Instrum. **14**, C09039 (2019).
[84] M.I. Kobayashi *et al.*, IEEE Trans. Instrum. Meas. **73**, 6010808 (2024).
[85] M.I. Kobayashi *et al.*, Nucl. Fusion **64**, 066026 (2024).
[86] C. Pazos *et al.*, arXiv.2406.01507 (2024).
[87] S. Avdic *et al.*, Nucl. Instrum. Meth. Phys. Res. A **565**, 742 (2006).
[88] G. D'Agostini, Nucl. Instrum. Meth. A **362**, 487 (1995).
[89] B. Malaescu, arXiv.0907.3791 (2009).
[90] G. Choudalakis, arXiv.1201.4612 (2012).
[91] G.N. Pendleton *et al.*, Nucl. Instrum. Meth. Phys. Res. A **364**, 567 (1995).
[92] Y. Kitayama *et al.*, Jpn. J. Appl. Phys. **63**, 032005 (2024).
[93] A.E. Shustov and S.E. Ulin, Phys. Procedia **74**, 399 (2015).
[94] V.V. Gaganov *et al.*, J. Instrum. **17**, T09001 (2022).
[95] S.A. Kuvin *et al.*, Phys. Rev. C **104**, 014603 (2021).
[96] H. Sakane *et al.*, Ann. Nucl. Energy **29**, 53 (2002).
[97] J. Liu *et al.*, Sci. Rep. **12**, 12022 (2022).
[98] M. Passeri *et al.*, Nucl. Instrum. Methods Phys. Res. A **1010**, 165574 (2021).
[99] O. Philip *et al.*, IEEE Trans. Nucl. Sci. **64**, 2683 (2017).
[100] T. Muroga *et al.*, Fusion Sci. Technol. **56**, 897 (2009).